Petrogenesis of arc-related serpentinized peridotites (Egypt): Insights into Neoproterozoic mantle evolution beneath the Arabian-Nubian Shield

Mohamed Zaki Khedr [a,*], Eiichi Takazawa [b], Christoph Hauzenberger [c], Akihiro Tamura [d], Shoji Arai [d], Robert James Stern [e], Tomoaki Morishita [d], Amr El-Awady [f]

[a] Department of Geology, Faculty of Science, Kafrelsheikh University, 33516 Kafrelsheikh, Egypt
[b] Geology Department, Faculty of Science, Niigata University, Niigata 950-2181, Japan
[c] Institute of Earth Sciences - NAWI Graz Geocenter, Karl-Franzens-Universität Graz, 28010 Graz, Austria
[d] Department of Earth Sciences, Kanazawa University, Ishikawa 920-1192, Japan
[e] Geosciences Department, University of Texas at Dallas, Richardson, TX 75083-0688, USA
[f] Geology Department, Faculty of Science, Zagazig University, Zagazig 44519, Egypt

ARTICLE INFO

ABSTRACT

Korab Kansi and Abu Dahr Neoproterozoic ophiolitic peridotites in the Southern Eastern Desert (SED) of Egypt, are parts of the largest ophiolitic nappes in the Arabian-Nubian Shield. They mainly comprise refractory harzburgites with minor dunites that are commonly altered to serpentinites and talc carbonates. Olivine relics in serpentinized peridotites of the two complexes have olivines with high forsterite ($Fo_{90.6-92.2}$) and NiO (0.39 wt%) and low MnO (0. 13 wt%) contents, similar to those of mantle olivines. High Mg# (0.91–0.95) of orthopyroxene is consistent with that of depleted harzburgites. Primary spinel Cr# (0.55–0.75) and TiO_2 contents (<0.04 wt%) of the two peridotite complexes are similar to forearc peridotite spinels. The estimated degree of partial melting of Korab Kansi peridotites (25–40% melting) is slightly lower than that of Abu Dahr (30–40% melting), consistent with modern forearc peridotites. Korab Kansi peridotites exhibit lower oxygen fugacity ($\Delta\log fO_2$, FMQ + 0.7 on average) and equilibrium temperature (610–710 °C) than those of Abu Dahr (T, 750–900 °C at $\Delta\log fO_2$, FMQ + 2.1), both suggesting subduction-modified peridotites. The low concentrations of incompatible elements, U-shaped REE patterns and high spinel Cr# of both peridotites indicate highly depleted mantle protoliths, reflecting multiple metasomatic and melting episodes in the mantle wedge. Enrichment of fluid mobile elements (e.g. B, Li, Th, U, Pb) relative to high-field strength elements (e.g. Nb, Ta, Ti, Zr) may reflect interaction between slab-derived fluids and peridotites. Calculated parental melts in equilibrium with Korab Kansi and Abu Dahr peridotite spinels have tholeiitic (MORB-like) and boninitic affinities, which were generated during proto-forearc spreading to a mature arc stage. Variations in melt compositions suggest a transitional setting from early proto-forearc spreading of mantle beneath Korab Kansi to the mature arc stage of Abu Dahr peridotites. Subduction initiation possibly started in the W and/or SW with proto-forearc spreading, and progressed to the E and/or NE where a mature arc stage with boninitic melts above an E- and/or SE-dipping subduction zone.

1. Introduction

Neoproterozoic ophiolites are widespread in the Central and South Eastern Deserts (SED) of Egypt (Fig. 1), and are part of the Arabian-Nubian Shield (ANS). The ANS represents the northern extension of the East African Orogen (550–850 Ma), and consists of juvenile Neoproterozoic crust associated with abundant ophiolites (Fritz et al., 2013). ANS ophiolites formed during the Tonian and Cryogenian (890–690 Ma) (e.g., Stern et al., 2004) and are associated with thrust faults and suture zones, including Abu Dahr and Korab Kansi ophiolites in the SED studied here (e.g. Khalil and Azer, 2007; Ahmed, 2013; Khedr and Arai, 2013, 2016, 2017). Eastern Desert ophiolites, were part of Mozambique Ocean floor, emplaced during closure of this ocean (Stern et al., 2004; Fritz et al., 2013).

Ophiolite peridotites reflect a wide range of melting and tectonic environments: 1) ones unrelated to forearcs and characterized by low degrees of partial melting, and 2) ones that formed in forearcs during subduction initiation and generated by high degrees of partial melting
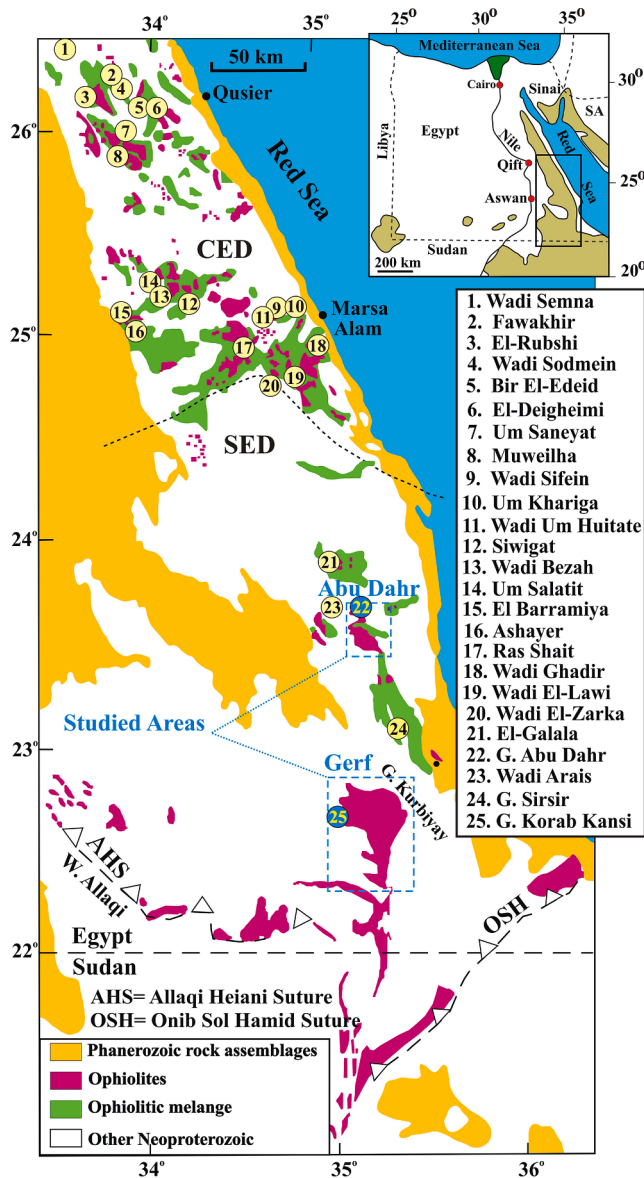

Fig. 1. (**a**) Map locations of 25 significant ophiolitic outcrops in the ED of Egypt showing locations of Abu Dahr and Korab Kansi ophiolite complexes (Shackleton, 1994).

preserve primary mantle textures. This study deals with the geology, petrography, chemistry of primary mantle minerals and bulk-rock chemistry of ultramafic rocks from two of the largest ANS ophiolitic nappes: Korab Kansi (Gerf nappe) and Abu Dahr. The aim of this study is to determine peridotite origin and tectonic setting and use this information to help constrain Neoproterozoic mantle geodynamic evolution beneath the northern ANS. This study sheds new light on variations of the Neoproterozoic mantle oxidation state (oxygen fugacity) with changing tectonic styles in the supra-subduction zone setting.

2. Locations and geologic setting

Korab Kansi and Abu Dahr (Fig. 1) are in the South Eastern Desert (SED) of Egypt, which is part of the Arabian Nubian Shield (ANS) that formed between East and West Gondwana (Fritz et al., 2013). The largest SED ophiolites occur as dismembered tectonized masses and mélanges that are parts of the Allaqi–Heiani–Gerf and Onib-Sol Hamed suture zones, including Korab Kansi (Fig. 1). The Korab Kansi ophiolite lies ~12 km west of the Gabal Gerf nappe, the largest ANS ophiolite (Fig. 1). Korab Kansi is 74 km southwest of Shalateen City, bounded by latitudes 22° 35 40 to 22° 42 39 N and longitudes 34° 57′ to 35° 3′ E (Fig. 2a). The Abu Dahr complex is the second largest ophiolitic body in the Eastern Desert, located about 90 km NE of Korab Kansi.

The Gerf terrane (including Korab Kansi) overrode the Gabgaba terrane to the south during an arc/arc collision (750–720 Ma) associated with N–S to NNE–SSW shortening (Kusky and Ramadan, 2002; Abdeen and Abdelghaffar, 2011). The Neoproterozoic Allaqi–Heiani Shear (AHS) zone (~730–700 Ma) is dominated by an E-W to NW-SE trending fold and thrust belt (Fig. 1) (Abdeen and Abdelghaffar, 2011), which resulted from the collision between Gerf and Gabgaba terranes, preceding the closure of Mozambique Ocean (Greiling et al., 1994). The Korab Kansi area is also affected by the N-S trending Hamisana shear zone (660–610 Ma) associated with E-W shortening and with a strong N–S extensional component. Strike–slip faults are the most conspicuous structural elements in the Korab Kansi area and trend E–W, ENE–WSW and NNW–SSE (Fig. 2a). E–W and ENE–WSW faults are common in the study area, representing one of the main tectonic trends in the Eastern Desert of Egypt (Youssef, 2003). A NNW-SSE sinistral slip fault passes through Wadi Seyet, separating Korab Kansi from Gabal Gerf (Fig. 2a). This fault is younger than the previously mentioned faults because it offsets dykes parallel to the first trends (Fig. 2a).

Korab Kansi covers about 200 km² and is composed of an ophiolitic assemblage, felsic to intermediate volcanic schists, the layered mafic–ultramafic intrusion (Khedr et al., 2020) and *syn*-tectonic granites (Fig. 2a). The ophiolitic assemblage is dominated by serpentinized peridotites (~70 km²) with less abundant metagabbros in the northwest (Fig. 2a). Korab Kansi and Gerf ophiolites were obducted over slightly older juvenile crust during terrane assembly by low-angle thrust faulting prior to the E-W assembly of Gondwanaland (~635 Ma) (Ali et al., 2010). In the northwestern Korab Kansi area, serpentinized peridotites are tectonically emplaced over metagabbros and felsic to intermediate volcanic schists across low-angle thrust faults (Fig. 2a). Small unmappable tectonic slices of metagabbros lie along the tectonic contact between ophiolitic units (Abdel-Gawad, 2002). This thrust zone shows intense shearing, stretching, mineral lineations and mylonitic deformation of ophiolitic rocks, as well as discordant beds above the thrust (Abdel-Gawad, 2002). In addition, layered mafic–ultramafic rocks and *syn*-tectonic granites in the south (Fig. 3a) intrude serpentinized peridotites. They show intrusive contacts with serpentinized peridotites, forming hydrous and prograde peridotites as a result of contact metamorphism. The relationship between dated Gebel Gerf ophiolitic gabbros (741 ± 21 Ma; Kröner et al., 1992) and associated Korab Kansi peridotites suggests a similar age.

Korab Kansi serpentinized peridotites and serpentinites are generally massive, except at the thrust contact with metagabbros. Some peridotites have large shiny porphyroblasts of orthopyroxene (Fig. 3b), and

(e.g., Furnes et al., 2014). The tectonic settings of ED ophiolites are debated. Different tectonic settings based on spinel chemistry are proposed: 1) mid-ocean ridges (e.g. Zimmer et al., 1995); 2) supra-subduction zones (SSZ) including forearc and arc settings (e.g. Azer and Khalil, 2005; Azer and Stern, 2007; Ahmed, 2013; Khedr and Arai, 2013, 2016, 2017) as well as back-arc basins (Abd El-Rahman et al., 2009). Ophiolitic ultramafic rocks in Egypt are commonly altered to serpentinite and talc carbonate due to metasomatism and/or metamorphism under greenschist conditions (e.g. Farahat et al., 2011; Khedr and Arai, 2013; Abdel-Karim et al., 2016). Consequently, primary mantle minerals are rare (Khedr and Arai, 2013); fortunately, Abu Dahr and Korab Kansi ultramafic rocks from the largest ophiolitic nappes in the ANS are relatively fresh and rich in primary mantle minerals.

Neoproterozoic mantle geodynamic evolution of SED ophiolites and the ANS need to be better understood. ED ophiolitic peridotites provide key constraints for understanding Neoproterozoic mantle geodynamic evolution beneath the ANS. Korab Kansi and Abu Dahr peridotites are especially important to study because they preserve primary mantle minerals such as olivine, orthopyroxene and chromian spinel, and
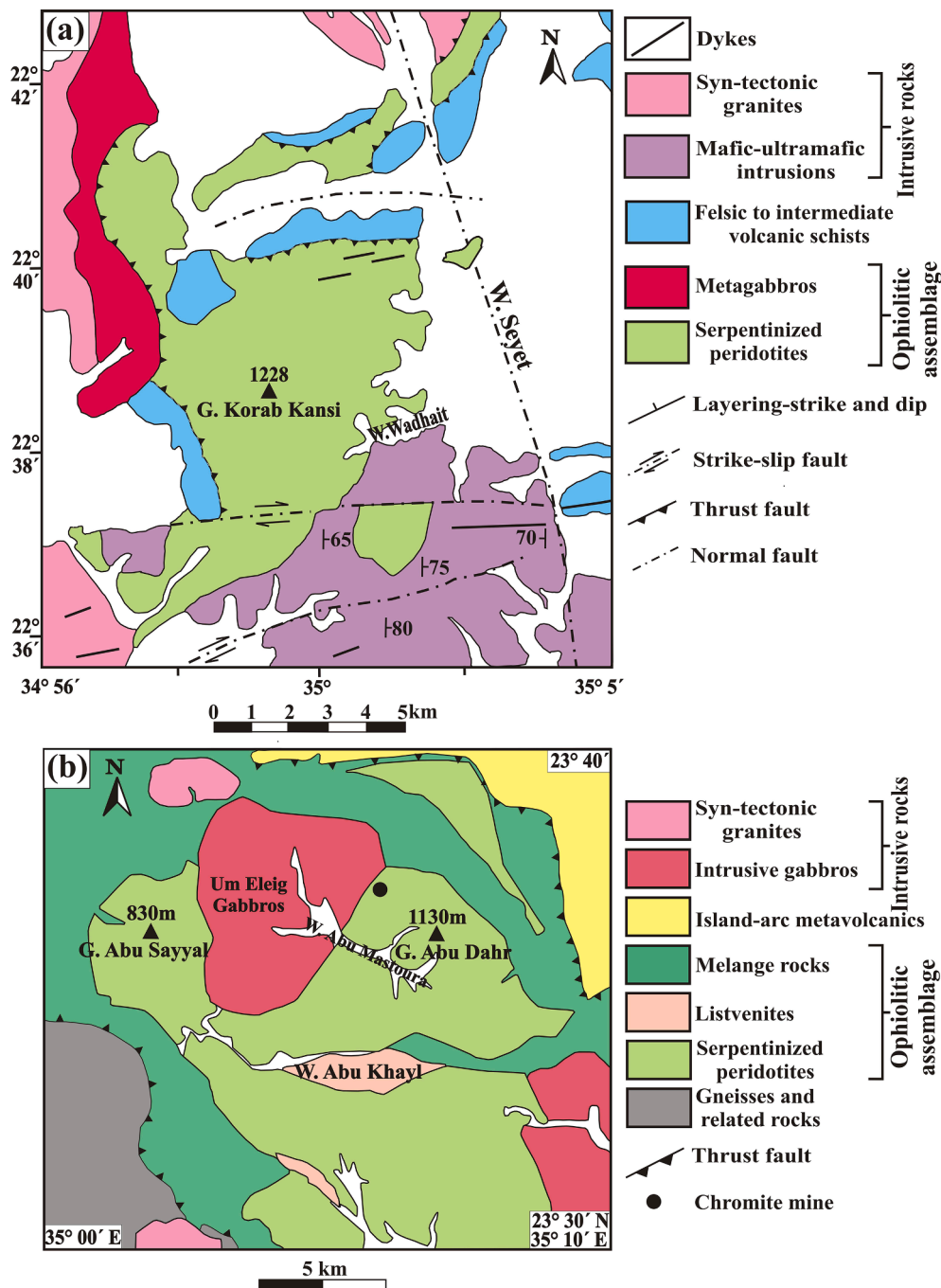
Fig. 2. Geological maps showing Korab Kansi and Abu Dahr ophiolites. (**a**) Geology of Korab Kansi area (Abdel-Gawad, 2002), (**b**) Geology of Abu Dahr area (Khedr and Arai, 2016; Abdel Halim et al., 2020).

sometimes contain small orthopyroxenite veinlets. Along shear zones, serpentinites are sheared, foliated (Fig. 3c) and partly to completely altered to buff colored talc-carbonate rocks, which occur as scattered patches, veins and sheets within serpentinite masses (Fig. 3d). Basaltic dykes with sharp intrusive contacts (Fig. 3e) intrude talc-carbonates and are displaced by normal faults (Fig. 3e). NE-SW dip-slip faults also cut the serpentinites, metavolcanic schists and *syn*-tectonic granites (Abdel-Gawad, 2002). These faults can be traced for about 100 m and exhibit a vertical displacement of about 1 m.

Abu Dahr is located ~90 km northeast of Korab Kansi (Fig. 1). The ophiolites in Abu Dahr cover about 150 km^2 and are bounded by latitudes 23° 30′ to 23° 40′ N and longitudes 35° 00′ to 35° 10′ E (Fig. 2b). The Abu Dahr area consists mainly of gneisses, ophiolitic assemblages,

island arc metavolcanics/metagabbro-diorite complex and syn- to late-tectonic granites (Khedr and Arai, 2013, 2016; Gahlan et al., 2015; Abdel Halim et al., 2020) (Fig. 2b). Thrusting of Abu Dahr ophiolitic assemblages over Beitan gneisses was toward the west and southwest. Ophiolitic assemblages include serpentinized peridotites with chromitite lenses along with listvenite and mélange rocks, which are mainly ophiolitic metavolcanics and ultramafic fragments mixed with metasedimentary rocks (Fig. 2b) (Khedr and Arai, 2016). The Abu Dahr area was affected by several deformation phases that produced dominant NW-SE trending anticlines and synclines and E-W trending faults (Abdel Khalek et al., 1992). The Abu Dahr ophiolitic nappe is the second largest in the SED after the Gerf nappe (Fig. 1). This dismembered ophiolite occurs as imbricated thrust sheets in the central part of the Zarqet
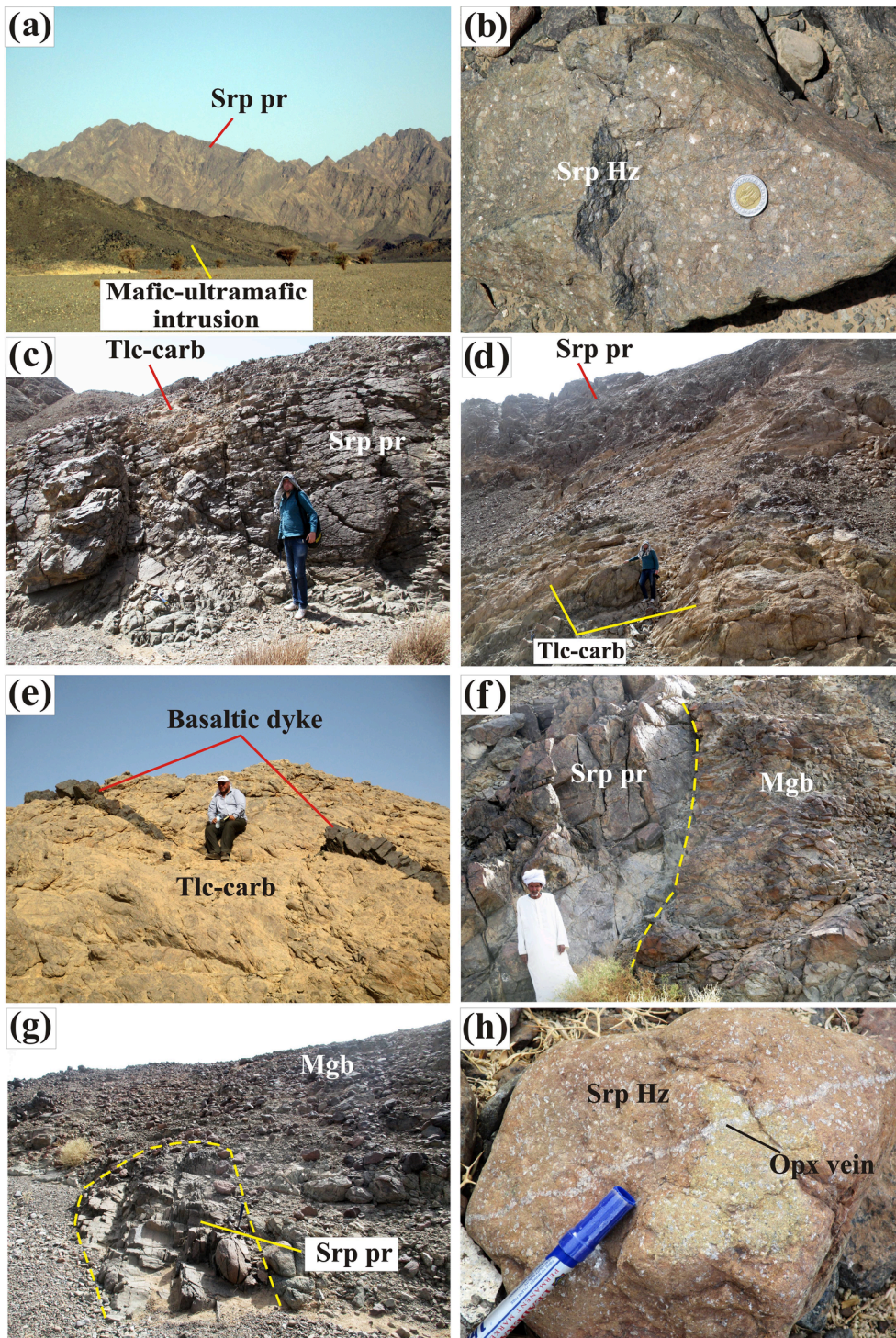
Fig. 3. Field photographs of Korab Kansi and Abu Dahr ophiolitic peridotites. (**a**) Sharp contact between the Korab Kansi mafic–ultramafic intrusion and serpentinized peridotites (Srp pr). (**b**) Shiny orthopyroxene (Opx) porphyroblastic crystals in Korab Kansi serpentinized harzburgites (Srp Hz). (**c**) Highly sheared serpentinized peridotites partly altered to talc-carbonates (Tlc-carb). (**d**) Sheets or patches of talc-carbonates along shear zones cutting Korab Kansi serpentinized peridotites. (**e**) Basaltic dyke cutting through Korab Kansi talc-carbonates and displaced by fault. (**f**) Tectonic contact between Abu Dahr ophiolitic metagabbros (Mgb) and serpentinized peridotites. (**g**) Boudins of Abu Dahr serpentinized peridotites contacted with ophiolitic metagabbros. (**h**) Opx veinlet traversing Abu Dahr serpentinized harzburgites.

Na'am–Rahaba ophiolite belt (Gahlan et al., 2015). Ophiolitic fragments are thrust over the 719–744 Ma Beitan gneiss (Ali et al., 2015) in the SW Abu Dahr area and are intruded by the island-arc metagabbro-diorite complex and syn- to late-tectonic granites (650–595 Ma; Moussa et al., 2008; Khedr and Arai, 2013, 2016)(Fig. 2b). From relationships with the Beitan gneiss, we conclude that the Abu Dahr ophiolite is > 744 Ma, consistent with the age of ANS ophiolites in general (Stern et al., 2004). Arc metavolcanic rocks are locally thrust over the ophiolitic association (Fig. 2b; Gahlan et al., 2015; Khedr and Arai, 2016).

The Abu Dahr ophiolite mantle section consists mainly of partially serpentinized harzburgites and subordinate more serpentinized dunites

(Khedr and Arai, 2016). These ultramafic rocks contain abundant podiform chromitites up to 50 m across (Ahmed, 2013; Khedr and Arai, 2016) and have a sharp tectonic contact with ophiolitic metagabbros (Fig. 3f). Serpentinized peridotites are sometimes found as dyke-like bodies in the lower parts of ophiolitic metagabbros (Fig. 3g). Partially serpentinized harzburgites with orthopyroxene porphyroblasts and small orthopyroxenite veinlets are common (Fig. 3h). Abdel Halim et al. (2020) noted that harzburgites are traversed by orthopyroxenite dykes and host small dunite-chromitite lenses. Some ultramafic rocks are altered to talc-carbonate and schistose serpentinite along shear zones. Serpentinized harzburgites are foliated with NW–SE to WNW–ESE

trends, parallel to regional structure (Gahlan et al., 2015). Concordant wehrlites, pyroxenites and gabbro layers above serpentinized dunites near the uppermost parts of the ophiolitic mantle section are interpreted as a fossil Moho (Gahlan et al., 2015).

More than 50 ultramafic-rock samples from the Korab Kansi complex and 78 samples from the Abu Dahr complex were collected and prepared for petrography and mineral chemistry. We collected ultramafic rocks from Korab Kansi mainly around Wadi Wadhait and west of Wadi Seyet
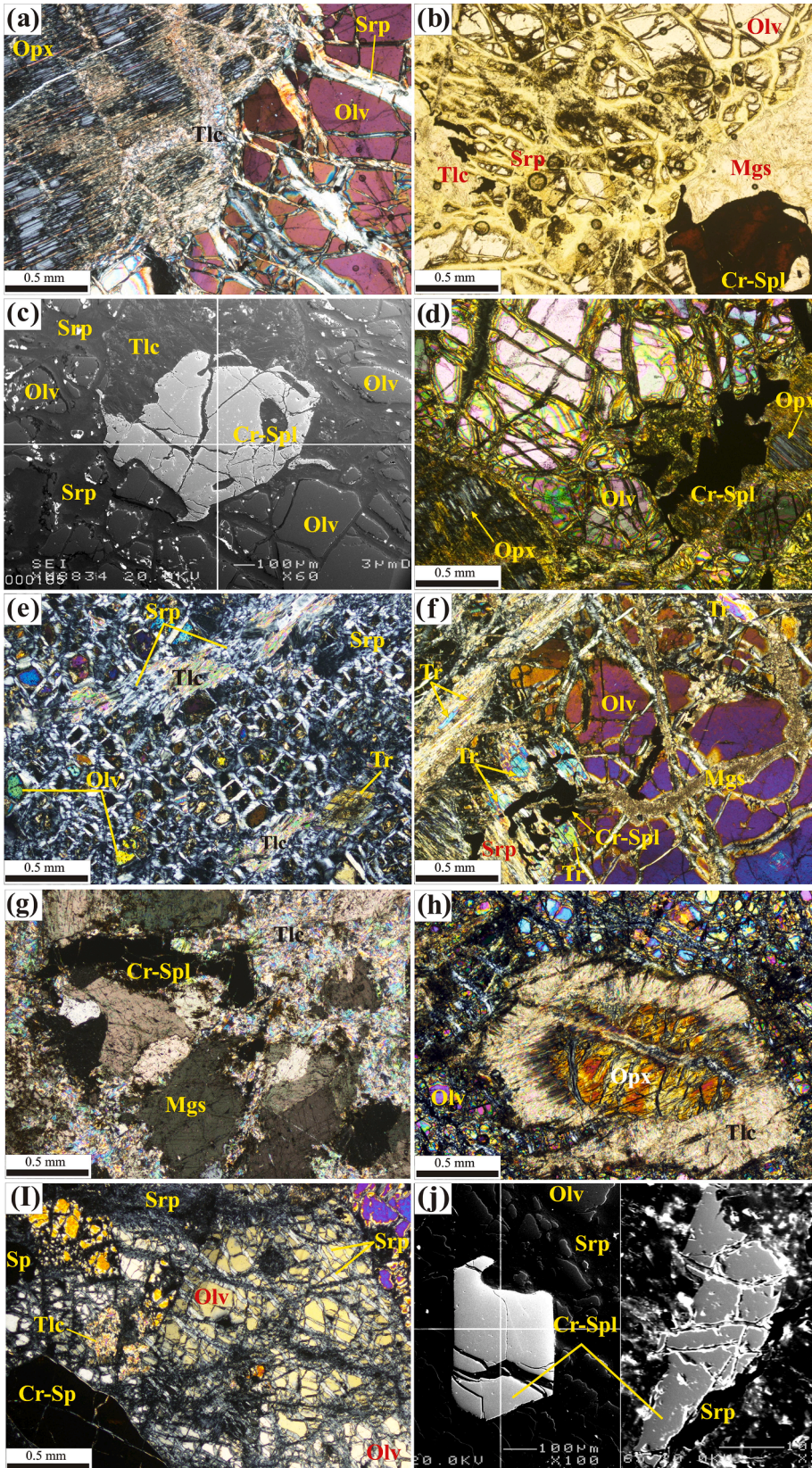

Fig. 4. Photomicrographs of Korab Kansi and Abu Dahr ultramafic rocks. All photos were taken under polarized light, except **b** under plane-polarized light and **c** and **j** (back scattered electron images: BSE). (**a**) Protogranular texture composed of prismatic Opx and equigranular olivine with talc and serpentine alteration along rims and cracks, Korab Kansi harzburgites. (**b**) Intact chromian spinel with deep red colored and homogenous olivine, showing protogranular texture for Korab Kansi serpentinized harzburgites. (**c**) Homogenous chromian spinel and primary olivine without opaque inclusions, Korab Kansi harzburgites. (**d**) Primary mantle minerals such as fresh olivine, laminated Opx and amoeboid or vermicular chromian spinel, forming massive harzburgites in Korab Kansi. (**e**) Mesh-textured serpentine surrounding olivine relics mixed with fibrous talc and rare tremolite, Korab Kansi serpentinized dunites. (**f**) Equigranular olivine veined with magnesite and prismatic tremolites around vermicular chromian spinel, Korab Kansi hydrous dunites. (**g**) Fibrous talc aggregates filling spaces between magnesite grains, Korab Kansi talc-carbonates. (**h**) Fresh core Opx altered along its periphery to talc and forming the corona-like texture, Abu Dahr harzburgites. (**i**) Chromian spinel and equigranular olivine partly altered along cracks into serpentine, Abu Dahr dunites. (**j**) Homogenous euhedral to subhedral chromian-spinel without alteration rims, Abu Dahr dunites. Abbreviations; Opx, orthopyroxene; Olv, olivine; Cr-Spl, chromian spinel; Srp, serpentine; Tlc, talc; Tr, tremolite; Fe-Ch, ferritchromite; Atg, antigorite; Mgs, magnesite. (For interpretation of the references to color in this figure legend, the reader is referred to the web version of this article.)

(Fig. 2a), beside the north part of G. Korab Kansi near the contact with metagabbros and metavolcanics. Most ultramafic rocks from the Abu Dahr complex were collected around Wadi Abu Mastoura, north of G. Abu Dahr and near the contact with Um Eleig gabbros (Fig. 2b).

3. Petrography

Korab Kansi and Abu Dahr serpentinized harzburgites (Fig. 4a-d, h) and subordinate dunites (Fig. 4e, i, j) preserve relict olivine, orthopyroxene (Opx), and chromian spinel (Cr-spinel). Korab Kansi harzburgites have more mantle mineral relics than those of Abu Dahr. Harzburgites are composed mainly of fresh olivine (~50–65 vol%), Opx (~20–25 vol %), serpentine matrix, Cr-spinel (<1 vol%) and rare bastite pseudomorphs of orthopyroxene (Fig. 4a-d; Supplement 1a, b). Serpentine, talc and carbonates are secondary (Fig. 4a-d). Olivines are mostly fresh equant grains (0.2 mm across) showing protogranular textures (Fig. 4a, d). They are homogenous and mostly free of opaque inclusions (Fig. 4a-d; Supplement 1a, b), showing the morphology of mantle olivine. Olivines are sometimes slightly serpentinized along cracks (Fig. 4b). Olivines peripheries are corroded by Opx with irregular contacts (Fig. 4a). Opx occurs as coarse prismatic crystals (1.5–3 mm; Fig. 4a) or as small interstitial grains (0.8 mm across) between olivines. Some Opx grains are partly to completely replaced by serpentine (bastite) and/or talc minerals (Fig. 4h; Supplement 1a, b); this is more common in Abu Dahr than in Korab Kansi peridotites. Relict Opx is sometimes found as islands in talc, forming corona-like structures (Fig. 4h). Most bastites preserve cleavages of precursor Opx and are composed mainly of lizardite. Chromian spinels are subhedral to anhedral in dunites (Fig. 4e, i, j) and anhedral in harzburgites (Fig. 4a-d, h). Primary chromian spinel, which is vermicular or amoeboid in shape (up to 1.2 mm; Fig. 4d) with red color (Fig. 4b), is associated with mantle Opx and olivine (Fig. 4b-d). Spinels are mainly homogenous (Fig. 4c; Supplement 1b) or have fresh cores (Fig. 4b), showing primary textures.

Serpentinized dunites consist of ~50–65 vol% olivine, ~30–40 vol% mesh-textured serpentine after olivine (Fig. 4e) and rare bastite after Opx (<5 vol%) with subordinate talc and Cr-spinel (Fig. 4e). Olivines (0.3–0.4 mm across) are mostly equant grains that are partly altered along cracks into chrysotile/lizardite (Fig. 4e). They are sometimes completely serpentinized, forming mesh textures (Fig. 4e). Serpentinized dunites are composed of serpentine minerals that form net-like textures around fresh olivine relics (Fig. 4e). Serpentine minerals are mainly lizardite/chrysotile and rarely antigorite in Abu Dahr, while Korab Kansi serpentinites have more antigorite. Cr-spinel in dunites (<3 vol%) is subhedral to anhedral (0.2–1 mm across) (Fig. 4i, j). Cr-spinel is sometimes pitted with silicate inclusions. A few Cr-spinel grains have fresh cores surrounded by ferritchromite rims.

A different kind of altered dunite is observed only in Korab Kansi, which we call hydrous dunites (Fig. 4f; Supplement 1c). These consist mainly of olivine (30–40 vol%), pseudomorph olivines (mesh-textured serpentines) (40–45 vol%), tremolite (~10 vol%) and talc (5–10 vol%) with rare Cr-spinel (<1 vol%) (Fig. 4f). Olivine occurs as rounded equigranular grains (0.5 mm across; Fig. 4f) or as cores in mesh-textured serpentines. These are sometimes dissected by networked veins of serpentine, forming interlocking textures. Serpentine is found as fine-dusty matrix and as fibers and veinlets, and is composed mainly of lizardite and chrysotile. Fibrous tremolite (0.2–0.4 mm) may crosscut olivine and serpentines (Fig. 4f). Talc occurs as fine flakes or paste with high interference colours. Cr-spinel is amoeboid between olivine grains (Fig. 4f).

Massive serpentinites consist mainly of non-pseudomorphic interpenetrating feather-like antigorite with subordinate olivine, fibrous chrysotile, talc, calcite, and Cr-spinel (Supplement 1d). Schistose and foliated serpentinites along shear zones are altered to talc-carbonate serpentinites and talc carbonates (Supplement 1e, f). Talc carbonate serpentinites consist of serpentine minerals (~55–60 vol%), magnesite (~30–35 vol%) and talc (~10 vol%) with rare opaque minerals (~3 vol %). Serpentine minerals are mostly fibrous interpenetrating antigorite with minor fine dusty lizardite. Talc occurs as paste or fine flakes mixed with serpentine matrix, while magnesite is found as cryptocrystalline veinlets, sparse crystals and granular aggregates.

Talc-carbonate rocks consist mainly of magnesite (~55 vol%) and talc (~40 vol%) with minor opaques (~5 vol%) such as chromian spinel, magnetite and sulphides (Fig. 4g; Supplement 1e, f). Magnesite is commonly pigmented with reddish iron oxide and occurs as granular aggregates, while talc fills spaces between magnesite (Fig. 4g). Cr-spinels are brecciated, fractured and mostly replaced by ferritchromite and magnetite along cracks and rims. Magnetite and pentlandite occur as fine specks and subhedral to euhedral disseminated crystals (Supplement 1e, f).

4. Analytical methods

Major-element contents of silicate minerals (265 analyzed points) and spinels (84 analyzed points) from Korab Kansi and Abu Dahr peridotites were analyzed by an electron microprobe (JXA-8800, JEOL) at Kanazawa University, Japan (Tables 1, 2; Supplement 2). Accelerating voltage, beam current, and beam diameter for silicate and spinel analyses were 20 kV, 20nA, and 3 μm, respectively. The data were corrected using ZAF. The values of Si, Cr, Fe, Ca, (K, Ti), Al, Mn, Na, Ni and Mg were determined and calibrated on the standards: quartz, eskolaite, fayalite, wollastonite, $KTiPO_5$, corundum, manganosite, jadite, nickel oxide and periclase, respectively. The diffracting crystals were TAP for Si, Al, Na and Mg; PETJ for Cr, Ca, K, and Ti; LIF for Fe, Mn and Ni. The detection limits (ppm) calculated by the microprobe soft-ware are Si (123), Cr (320), Fe (195), Ca (115), K (98), Ti (199), Al (117), Mn (198), Na (138), Ni (178) and Mg (119). Mg# is Mg/(Mg + total Fe) atomic ratio for bulk rocks and silicates; we assumed all Fe in silicates was ferrous. Cr-number (Cr#) and Mg-number (Mg#) of spinels are Cr/ (Cr + Al) and Mg/(Mg + Fe^{2+}) atomic ratios, respectively. Ferrous and ferric iron contents of chromian spinel were calculated assuming spinel stoichiometry. Y_{Cr}, Y_{Al} and Y_{Fe} are the atomic proportions of Cr, Al and Fe^{+3}, respectively, to trivalent cations, (Cr + Al + Fe^{+3}).

Trace-element contents (24 spots) of chromian spinel and Opx were obtained in-situ by laser ablation-inductively coupled plasma-mass spectrometry (LA-ICP-MS) using a quadrupole ICP–MS (Agilent 7500a) coupled to a 213 nm Nd:YAG laser ablation system (New Wave Research UP213) at Niigata University, Japan. Trace element contents of olivine, Opx and tremolite were determined by laser-ablation (193 nm ArF excimer: MicroLas GeoLas Q-plus)–inductively coupled plasma mass spectrometry in Kanazawa University, Japan (Supplement 3). Analyses were achieved by ablating 100 μm diameter spots for Opx, olivine, tremolite and chromian spinel. All analyses were carried out at 6 Hz with energy density of 8 J/cm^2 per pulse with energy density of 8 J/cm^2 per pulse. NIST 612 glass was used as an external standard for quality control and ^{29}Si was used as an internal standard for all silicates based on SiO_2 concentration obtained by electron microprobe. ^{27}Al and ^{26}Fe were used as internal standards for chromian spinel based on Al_2O_3 and FeO concentrations obtained by electron microprobe. NIST 614 glass (secondary standard) was measured for quality control of each analysis. Analyses precision exceeded 5% for most elements, except Sc, Cr and Ni for which it was > 10%. Accuracy and data quality were calculated based on reference material NIST 614.

Nine samples with abundant mantle mineral relics were selected for major and trace element analyses: two dunites and seven harzburgites. These samples were analyzed for major and trace elements at NAWI Graz Geocenter- Institute of Earth Sciences, Petrology and Geochemistry, University of Graz, Austria (Table 3). The X-ray fluorescence (XRF) spectrometer (Bruker Pioneer S4) was used for analyzing major and selected trace elements (Cr, Ni, V). Loss on ignition (LOI) was determined by heating the powdered rock material to 1025 °C for >1 h. About 80 international reference materials were used for calibrating the Bruker Pioneer S4. Analytical methods and international reference materials

Table 1
Representative microprobe analyses of olivine, orthopyroxene, serpentine, tremolite and talc from Abu Dahr and Korab Kansi serpentinized peridotites.

	Abu Dahr				Korab Kansi						Abu Dahr		Korab Kansi			Abu Dahr	Korab Kansi	Korab Kansi	Korab Kansi	Korab Kansi
Rock Name	Serpentinized harzburgite		Serpentinized dunite		Serpentinized harzburgite		Prograde dunite		Hydrous dunite		Serpentinized harzburgite		Serpentinized harzburgite (Spr. Hrz)					Prograde dunite	Spr. Hrz	Hydrous dunite
Sample No.	Rh75r	Rh73r	Rh74r	Rh82r	Sn18r	Sn32r	Sn30r	sn50r	Sn38r	Sn38r	Rh75r	Rh72r	Sn32r	Sn-37r	Sn-24r	Rh78r	Sn32r	Sn30r	Sn19t	Sn38r
Mineral	Olivine										Orthopyroxene					Serpentine (Bastite)	Serpentine	Talc	Tremolite	
SiO$_2$	41.09	40.85	41.28	40.97	40.50	41.39	41.61	41.51	41.14	40.64	57.20	58.95	57.86	55.80	55.86	37.43	34.69	61.42	57.54	57.71
TiO$_2$	0.00	0.00	0.00	0.00	0.00	0.00	0.00	0.00	0.00	0.01	0.00	0.00	0.00	0.00	0.03	0.00	0.01	0.03	0.01	0.00
Al$_2$O$_3$	0.00	0.00	0.00	0.00	0.00	0.00	0.00	0.00	0.00	0.00	1.30	1.04	2.00	2.05	2.05	1.36	0.00	0.10	1.09	0.63
Cr$_2$O$_3$	0.00	0.00	0.00	0.00	0.00	0.00	0.11	0.00	0.00	0.00	0.52	0.49	0.67	0.74	0.79	0.62	0.00	0.02	0.39	0.17
FeO^t	8.43	8.40	7.95	7.95	8.85	8.66	4.55	4.62	7.78	8.00	4.80	5.42	4.24	5.54	5.12	4.78	6.55	0.89	1.43	1.53
MnO	0.13	0.11	0.12	0.12	0.12	0.14	0.10	0.15	0.06	0.16	0.13	0.12	0.11	0.14	0.13	0.13	0.12	0.00	0.06	0.02
MgO	50.43	50.25	50.07	51.50	49.50	50.75	53.04	53.56	50.66	50.25	32.59	34.36	33.02	34.15	34.44	36.02	40.03	31.42	23.57	23.56
NiO	0.40	0.41	0.36	0.37	0.35	0.36	0.39	0.46	0.38	0.27	0.09	0.07	0.09	0.10	0.13	0.07	0.33	0.01	13.11	12.59
CaO	0.00	0.01	0.01	0.00	0.00	0.00	0.00	0.00	0.00	0.00	4.27	0.71	0.98	1.60	0.98	0.06	0.00	0.01	0.51	0.14
Na$_2$O	0.01	0.01	0.00	0.01	0.00	0.00	0.00	0.01	0.00	0.00	0.00	0.00	0.00	0.00	0.00	0.00	0.00	0.00	0.01	0.02
K$_2$O	0.01	0.00	0.00	0.00	0.00	0.00	0.00	0.00	0.00	0.00	0.00	0.08	0.09	0.10	0.13	0.00	0.00	0.19	0.12	0.07
Total	100.5	100.0	99.8	100.9	99.3	101.3	99.8	100.3	100.0	99.3	100.9	101.3	100.0	100.1	99.5	80.5	81.7	94.1	97.8	96.4
Wo	–	–	–	–	–	–	–	–	–	–	7.98	1.34	1.95	2.98	1.85	–	–	–	–	–
En	–	–	–	–	–	–	–	–	–	–	84.82	90.47	91.30	88.74	90.42	–	–	–	–	–
Fo	91.30	91.32	91.71	91.92	90.77	91.14	95.31	95.24	92.01	91.65	–	–	–	–	–	–	–	–	–	–
Mg#	0.91	0.91	0.92	0.92	0.91	0.91	0.95	0.95	0.92	0.92	0.92	0.92	0.93	0.92	0.92	0.93	0.92	0.98	0.97	0.96

Total iron as FeOt; Spr dunite: Serpentinized dunite; Spr. Hrz: Serpentinized harzburgite; Wo = Ca/(Ca + Mg + Fe + Mn); En = Mg/(Mg + Ca + Fe + Mn); Fo = 100*Mg/(Mg + Fe); Mg# = Mg/(Mg + Fe) atomic ratio.

BNV-1, GSP-2, MGL-GAS and OPY-1 as standards were described in detail by Khedr et al. (2020). Trace and REE were measured by using about 50 mg of sample powder that was dissolved and mixed with 1 ml HNO$_3$ and 2 ml HF in a capped Savilex teflon beaker. Mixture was left on a hotplate at ~160 °C for more than two days. After drying, the samples were diluted with 2 ml 7.5 M HNO$_3$. About 330 μl of the sample was analyzed using an Agilent 7700 quadrupole inductively mass spectrometer (ICP-MS) at the Institute of Chemistry -Analytical Chemistry, University of Graz, Austria. The standards used were international reference material BHVO-2 and JR-2. To ensure analytical accuracy and quality control, GS-N, JB-1b, and OPY-1 were measured as external standards. The elements Ge, In and Re were used for internal drift correction.

5. Mineral chemistry

Olivine in Korab Kansi and Abu Dahr peridotites is forsterite (Fo$_{90.6-92.2}$; Table 1; Supplement 2). These high olivine Fo contents are consistent with those of Alpine peridotites (Fo$_{90–92}$ after Pearce et al., 1984) and are very similar to other (Fo$_{89-94}$) of ED ophiolitic peridotites (e.g. Azer and Stern, 2007; Khalil and Azer, 2007; Khedr and Arai, 2013, 2017) (Fig. 5a). On the other hand, olivine in Korab Kansi prograde dunites has unusually high Fo$_{94.9-95.9}$ content, similar to low-pressure olivines (Fo$_{91.5-96.5}$) in Happo-O'ne (central Japan) prograde peridotites (Khedr and Arai, 2012) (Fig. 5a, b; Table 1). This olivine plots in the field of low-T olivine in prograde peridotites (Khedr and Arai, 2012) (Fig. 5b).

Orthopyroxenes (Opxs) in Korab Kansi and Abu Dahr harzburgites are mainly enstatite with high Mg#, ranging from 0.91 to 0.93 (Table 1; Supplement 2). Opx in Korab Kansi harzburgites has higher average Al$_2$O$_3$ (1.93 wt%) and Cr$_2$O$_3$ (0.71 wt%), but lower CaO (1.22 wt%) than those of Abu Dahr harzburgites, i.e., Al$_2$O$_3$, 1.2 wt%; Cr$_2$O$_3$, 0.5 wt%; CaO, 1.8 wt% (Supplement 2). Korab Kansi Opx is chemically similar in Al$_2$O$_3$, Cr$_2$O$_3$ and CaO contents to those of Opxs in SED serpentinized harzburgites, i.e, 2.3 wt% Al$_2$O$_3$, 0.74 wt% Cr$_2$O$_3$ and 1.1 wt% CaO (Khedr and Arai, 2016).

Tremolite with high Mg# (0.96) is observed mainly in Korab Kansi hydrous dunites and to lesser extent in harzburgites. Undetectable TiO$_2$ and low Al$_2$O$_3$ contents (0.85 wt% on average; Supplement 2) indicate a secondary origin (e.g., Khedr and Arai, 2012) as an alteration product of Opx. This tremolite has similar SiO$_2$ (57.5–57.7 wt%) and Na$_2$O (0.14–0.5 wt%) contents to those of tremolites in Happo O'ne prograde peridotites, i.e., 56.95–59.88 wt% SiO$_2$ and 0.03–0.29 wt% Na$_2$O (Khedr and Arai, 2012).

Serpentine minerals have variable contents of SiO$_2$ (34.7–37.5 wt%), Al$_2$O$_3$ (0.01–2.74 wt%), Cr$_2$O$_3$ (0.01–0.76 wt%), FeO (2.0–6.5 wt%), MnO (bdl–0.16 wt%), MgO (34.2–40.0 wt%) and NiO (0.06–0.35 wt%) (Table 1; Supplement 2). Bastite after Opx has higher average contents of Al$_2$O$_3$ (1.45 wt%), Cr$_2$O$_3$ (0.33 wt%), FeO (5.42 wt%) and MnO (0.12 wt%), but lower contents of SiO$_2$ (37.77 wt%), NiO (0.08 wt%) and Mg# (0.92) than mesh-textured serpentine after olivine, i.e., Al$_2$O$_3$ and Cr$_2$O$_3$ (<0.1 wt%), FeO (4.3 wt%), MnO (0.07 wt%) (Table 1). Cr$_2$O$_3$ and NiO contents of serpentine minerals reflect their precursor Opx and olivine (Fig. 5f). Talc in dunites and harzburgites has high Mg# (0.97–0.98) (Table 1).

Chromian spinel in Abu Dahr peridotites and serpentinites has slightly higher Cr# (0.6–0.74; 0.68 on average) and Mg# (0.32–0.54; 0.46 on average) than spinel in Korab Kansi peridotites, i.e., spinel Cr#= 0.54–0.76 with average 0.6; Mg#= 0.34–0.5 with average 0.44 (Table 2; Supplement 2). Spinel Cr# of Abu Dahr dunites (Cr#= 0.71 on average) and harzburgites (Cr#= 0.66) is higher than that of Korab Kansi (dunite spinel Cr#= 0.65; harzburgite spinel Cr#= 0.57 on average) (Fig. 6b, e, f; Supplement 2). The investigated spinel Cr# is lower than that of SED harzburgites (Cr#= 0.8 on average) and dunites (Cr#= 0.83) (Ahmed, 2013; Khedr and Arai, 2013, 2016; Abdel-Karim et al., 2016; Fig. 6f). It has low MnO (0.18–0.52 wt%) (Fig. 6b), TiO$_2$ (<0.05 wt%) (Fig. 6c, d),

Table 2

Representative microprobe analyses of chromian spinels, ferritchromite and magnetite from Abu Dahr and Korab Kansi serpentinized peridotites.

Area	Abu Dahr							Korab Kansi														
Rock	Serpentinized harzburgite				Serpentinized dunite			Serpentinized harzburgite				Prograde dunite		Hydrous dunite	Talc-carbonate		Prograde dunite				Srp Hrz	Talc-carbonate
Sample	Rh.75r	Rh.75r	Rh.73r	Rh.72r	Rh.74r	Rh.74r	Rh82r	Sn18r	Sn25r	Sn32r	Sn-36r	Sn29r	Sn29r	Sn38r	Sn55r	Sn55r	Sn30r	Sn30r	Sn30r	sn50r	Sn-36r	Sn55r
Mineral	Chromian spinel														Ferritchromite					Magnetite		
SiO_2	0.00	0.00	0.03	0.00	0.00	0.00	0.00	0.00	0.00	0.00	0.00	0.00	0.00	0.00	0.01	0.00	0.00	0.00	0.00	0.00	0.60	0.00
TiO_2	0.00	0.00	0.00	0.00	0.00	0.00	0.00	0.00	0.00	0.00	0.00	0.00	0.00	0.00	0.02	0.00	0.01	0.00	0.00	0.02	0.00	0.03
Al_2O_3	19.82	21.04	17.62	17.84	13.97	14.29	15.94	23.57	24.84	23.24	23.02	19.95	23.91	19.66	13.12	12.96	1.09	0.67	0.52	0.04	0.00	0.01
Cr_2O_3	47.29	46.53	50.41	48.96	53.94	54.49	52.69	46.02	44.27	46.88	45.71	49.16	44.37	45.65	54.10	54.12	18.68	16.71	10.24	0.29	0.00	0.00
FeO^t	22.58	22.80	22.13	23.38	23.30	20.80	20.20	21.15	20.36	20.04	21.37	23.35	23.06	24.33	31.87	32.02	67.89	72.28	76.21	87.20	86.44	78.53
MnO	0.32	0.37	0.37	0.47	0.47	0.30	0.36	0.39	0.34	0.35	0.41	0.46	0.40	0.37	0.24	0.20	0.38	0.26	0.31	0.73	0.78	0.00
MgO	9.82	9.38	9.81	8.36	7.81	9.84	10.15	9.09	10.28	9.97	9.23	7.65	8.18	9.01	1.93	1.77	4.44	3.96	3.09	1.41	0.32	0.13
NiO	0.07	0.04	0.02	0.02	0.03	0.03	0.06	0.00	0.07	0.03	0.00	0.00	0.00	0.04	0.00	0.00	0.77	0.86	1.16	1.08	0.32	1.67
CaO	0.00	0.00	0.00	0.00	0.04	0.00	0.00	0.00	0.00	0.00	0.00	0.00	0.00	0.00	0.00	0.00	0.00	0.00	0.00	0.00	0.00	0.13
Na_2O	0.03	0.00	0.00	0.02	0.00	0.01	0.00	0.02	0.05	0.00	0.03	0.02	0.04	0.00	0.02	0.04	0.00	0.00	0.00	0.00	0.00	0.10
K_2O	0.00	0.00	0.00	0.00	0.00	0.00	0.00	0.00	0.00	0.00	0.00	0.00	0.00	0.00	0.00	0.00	0.00	0.00	0.00	0.00	0.00	0.04
Total	99.93	100.15	100.39	99.06	99.56	99.75	99.40	100.25	100.21	100.53	99.76	100.60	100.00	99.05	101.29	101.12	93.25	94.73	91.53	90.77	88.46	80.63
Fe(ii)	4.20	4.38	4.20	4.64	4.80	4.11	3.99	4.52	4.12	4.22	4.45	4.97	4.82	4.46	7.16	7.23	5.74	5.99	6.22	1.20	1.28	1.29
Fe(iii)	0.59	0.44	0.52	0.45	0.36	0.41	0.37	0.00	0.10	0.00	0.05	0.03	0.04	0.77	0.11	0.10	11.21	11.87	13.33	2.62	2.61	2.60
Cr#	0.62	0.60	0.66	0.65	0.72	0.72	0.69	0.57	0.54	0.58	0.57	0.62	0.55	0.61	0.73	0.74	0.92	0.94	0.93	0.85	0.00	0.00
Mg#	0.44	0.42	0.44	0.39	0.37	0.46	0.47	0.43	0.48	0.47	0.44	0.37	0.39	0.44	0.10	0.09	0.29	0.26	0.22	0.08	0.02	0.01
Fe#	0.56	0.58	0.56	0.61	0.63	0.54	0.53	0.57	0.53	0.53	0.56	0.63	0.61	0.60	0.90	0.91	0.71	0.74	0.78	0.92	0.98	0.99
YCr	0.59	0.58	0.64	0.63	0.71	0.70	0.67	0.57	0.54	0.58	0.57	0.62	0.55	0.58	0.73	0.73	0.31	0.28	0.19	0.00	0.00	0.00
YFe + 3	0.04	0.03	0.03	0.03	0.02	0.03	0.02	0.00	0.01	0.00	0.00	0.00	0.00	0.05	0.01	0.01	0.66	0.70	0.80	0.99	1.00	1.00
YAl	0.37	0.39	0.33	0.34	0.27	0.27	0.30	0.43	0.45	0.42	0.43	0.38	0.44	0.37	0.26	0.26	0.03	0.02	0.01	0.00	0.00	0.00

Total iron as FeOt; Srp hzb: Serpentinized harzburgite; Mg# = Mg/(Mg + Fe2+); Cr# = Cr/(Cr + Al) atomic ratio. YCr, YAl and YFe are the atomic ratios of Cr, Al and Fe^{3+}, respectively, to trivalent cations (Cr + Al + Fe^{3+}).

8

Table 3
Major (wt.%) and trace element (ppm) contents of the studied serpentinzed peridotites.

Area	Abu Dahr		Korab Kansi					Prograde dunites	
Rock name	Serpentinized harzburgites								
Sample No	Rh.72	Rh-81	Sn.18	Sn.25	Sn.32	Sn.37	Sn.40	Sn.30	Sn.50
SiO_2	40.250	39.490	38.706	39.712	39.633	39.537	38.936	36.966	40.320
TiO_2	0.010	0.010	0.011	0.011	0.013	0.010	0.012	0.012	0.012
Al_2O_3	0.350	0.270	0.456	0.532	0.492	0.438	0.491	0.348	0.509
FeO*	7.610	7.580	7.882	8.020	8.067	8.302	7.637	7.967	7.145
MnO	0.106	0.101	0.111	0.113	0.115	0.115	0.109	0.105	0.099
MgO	40.560	41.590	40.137	40.453	40.616	41.800	39.441	38.165	37.809
CaO	0.480	0.290	0.340	0.480	0.481	0.398	0.435	0.239	0.321
Na_2O	0.010	0.010	<0.02	<0.02	<0.02	<0.02	<0.02	<0.02	<0.02
K_2O	0.010	0.010	<0.02	<0.02	<0.02	<0.02	<0.02	<0.02	<0.02
P_2O_5	0.002	0.002	0.008	0.007	0.007	0.007	0.007	0.007	0.007
Cr_2O_3	0.278	0.259	0.321	0.367	0.371	0.353	0.413	0.320	0.357
NiO	0.312	0.273	0.294	0.298	0.299	0.311	0.285	0.294	0.285
LOI	8.950	9.450	10.770	9.088	8.996	7.742	11.251	14.433	12.260
Total	98.928	99.336	99.038	99.081	99.091	99.013	99.015	98.857	99.124
Mg#	0.913	0.916	0.910	0.909	0.909	0.909	0.911	0.905	0.913
FeO*/ MgO	0.188	0.182	0.196	0.198	0.199	0.199	0.194	0.209	0.189
Al_2O_3/SiO_2	0.009	0.007	0.012	0.013	0.012	0.011	0.013	0.009	0.013
MgO/SiO_2	1.008	1.053	1.037	1.019	1.025	1.057	1.013	1.032	0.938
Trace elements (ppm)									
Li	0.483	0.584	0.419	0.244	0.334	0.281	0.614	0.799	0.624
B	5.004	4.885	3.970	3.771	3.367	3.139	4.148	6.412	5.435
Sc	7.158	4.407	5.686	6.138	6.349	5.808	7.994	6.768	6.263
V	32.857	26.603	25.641	25.694	24.073	25.091	27.401	25.205	28.311
Cr	3338.9	2743.9	2199.0	2511.3	2541.0	2414.3	2824.2	2192.8	2442.8
Co	112.8	108.1	109.2	108.6	107.9	114.7	104.5	109.7	98.8
Ni	2410.5	2517.1	2533.3	2512.2	2503.9	2655.9	2355.9	2441.7	2299.1
Cu	1.121	1.360	1.914	4.139	1.712	2.672	3.177	3.636	1.396
Zn	41.137	34.437	40.444	33.418	35.237	37.599	35.496	36.597	55.193
Ga	0.373	0.277	0.242	0.277	0.209	0.183	0.308	0.275	0.235
As	0.192	0.355	< 0.500	< 0.500	< 0.500	< 0.500	< 0.500	< 0.500	< 0.500
Rb	< 0.050	< 0.050	0.082	0.076	0.099	0.112	0.085	0.207	0.197
Sr	0.264	1.543	0.703	1.728	1.968	0.782	1.680	3.407	3.989
Y	0.023	0.020	0.015	0.022	0.019	0.012	0.009	0.019	0.015
Zr	0.044	0.042	0.093	0.098	0.110	0.120	0.098	0.106	0.130
Nb	0.086	0.086	0.097	< 0.100	< 0.100	0.099	< 0.100	< 0.100	< 0.100
Cs	0.008	0.008	< 0.100	< 0.100	< 0.100	< 0.100	< 0.100	< 0.100	< 0.100
Ba	0.184	0.377	0.664	3.006	0.784	0.491	0.825	1.547	1.096
La	< 0.01	< 0.01	0.006	0.028	0.008	0.004	0.003	0.017	0.006
Ce	0.004	0.005	0.011	0.056	0.016	0.008	0.006	0.043	0.011
Pr	<0.005	<0.005	0.002	0.007	0.002	0.001	0.001	0.004	0.001
Nd	<0.005	<0.005	0.006	0.028	0.009	0.005	0.003	0.015	0.005
Sm	<0.005	<0.005	0.003	0.007	0.002	0.004	0.002	0.005	0.003
Eu	0.002	0.002	< 0.001	0.002	< 0.001	< 0.001	< 0.001	0.001	0.001
Gd	<0.005	<0.005	0.002	0.006	0.004	0.003	0.002	0.005	0.003

| Area	Abu Dahr		Korab Kansi					Prograde dunites	
Rock name	Serpentinized harzburgites								
Sample No	Rh.72r	Rh.81r	Sn.18r	Sn.25r	Sn.32r	Sn.37r	Sn.40r	Sn.30r	Sn.50r
Trace elements (ppm)									
Tb	0.001	0.001	< 0.001	< 0.001	< 0.001	< 0.001	< 0.001	< 0.001	< 0.001
Dy	0.001	0.001	0.003	0.003	0.003	< 0.002	< 0.002	0.003	< 0.002
Ho	0.001	0.001	< 0.001	0.001	< 0.001	< 0.001	< 0.001	< 0.001	< 0.001
Er	0.003	0.003	0.003	0.004	0.003	0.003	0.003	0.003	0.003
Tm	0.001	0.001	0.001	< 0.001	< 0.001	< 0.001	< 0.001	< 0.001	< 0.001
Yb	0.008	0.005	0.009	0.010	0.009	0.008	0.007	0.005	0.009
Lu	0.009	0.002	0.003	0.003	0.002	0.003	0.003	0.002	0.003
Hf	0.017	0.016	< 0.01	< 0.01	< 0.01	< 0.01	< 0.01	< 0.01	< 0.01
Ta	0.037	0.032	0.012	0.014	0.014	0.016	0.012	< 0.01	< 0.01
Pb	0.076	0.050	< 0.100	0.677	< 0.100	0.102	< 0.100	< 0.100	0.151
Th	0.029	0.026	0.730	0.103	0.039	0.030	0.023	0.052	0.017
U	0.001	0.001	0.007	0.005	0.005	0.002	0.002	0.010	0.002
ΣREE	0.030	0.022	0.049	0.154	0.059	0.039	0.030	0.104	0.044
(La/Gd)N	–	–	3.00	4.00	1.50	1.00	1.00	2.33	1.50
(Lu/Gd)N	–	–	12.00	4.00	4.00	6.00	12.00	2.67	6.00
(B/Zr)N	–	–	1323	1257	1122	1046	1383	2137	1812
(B/Lu)N	128.23	543.33	330.75	314.25	374.00	261.50	345.75	712.33	453.00
(Zr/Hf)N	0.008	0.008	–	–	–	–	–	–	–
(Nb/Ta)N	0.140	0.162	0.455	–	–	0.347	–	–	–
Ni/Co	21.38	23.28	23.19	23.12	23.22	23.15	22.55	22.26	23.28
Nb/Ta	2.36	2.66	8.31	–	–	6.19	–	–	–
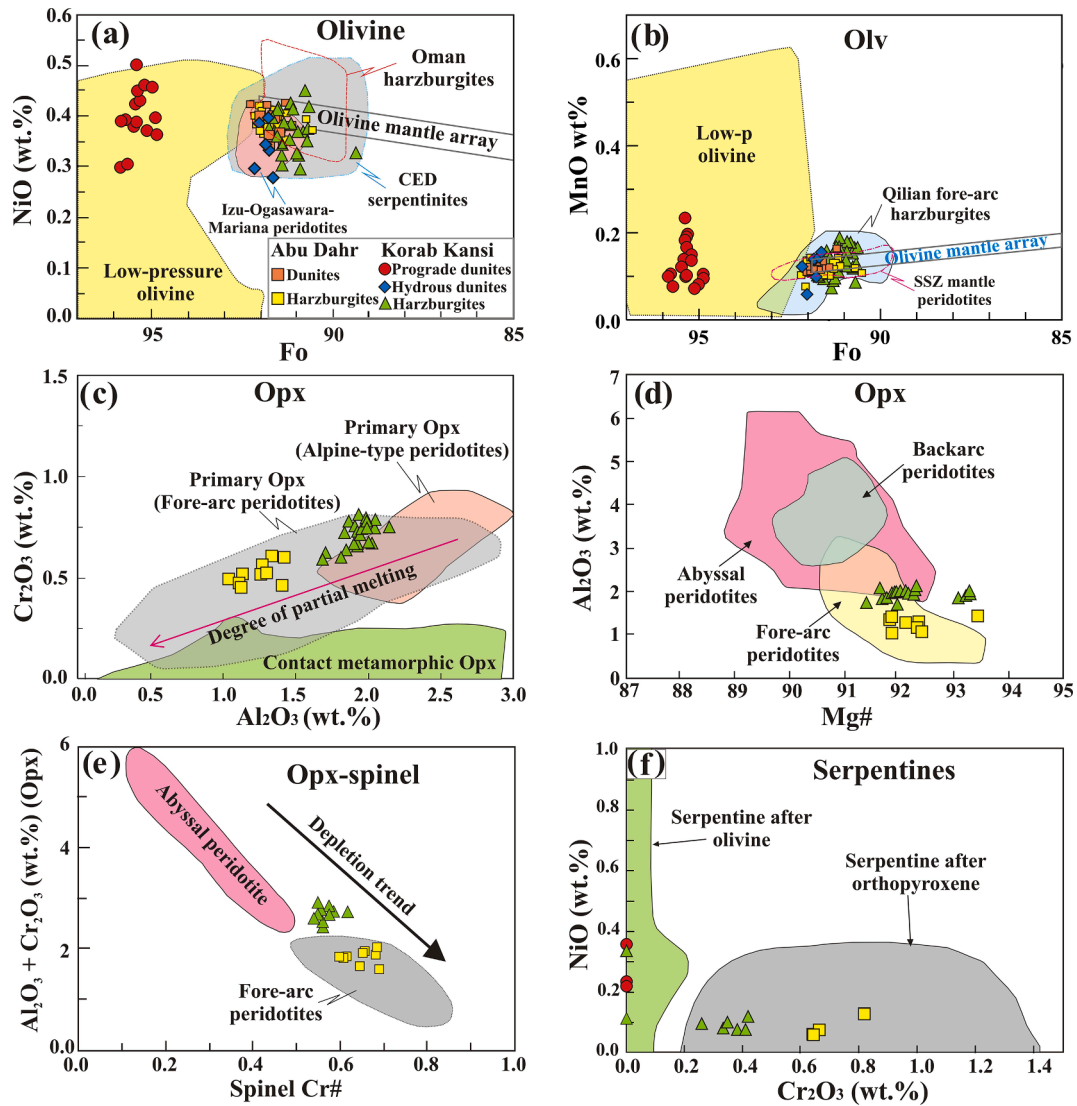
Fig. 5. (**a, b**) Forsterite (Fo) versus NiO (wt%) and MnO contents of olivines in serpentinized harzburgites, dunites and prograde dunites. Fields of olivine mantle array (Takahashi et al., 1987), CED serpentinites (Khedr and Arai, 2017), low-P olivine (Khedr and Arai, 2012), Izu-Ogasawara-Mariana peridotites (Ishii et al., 1992), and primary olivine from Oman harzburgites (Takazawa et al., 2003; Khedr et al., 2014) are shown for comparison. Olivines in Qilian forearc harzburgites of NW China (Song et al., 2009) and olivines in SSZ mantle peridotites from Mugla of SW Turkey (Uysal et al., 2012) are also shown for comparison. (**c, d**) Al_2O_3 versus Cr_2O_3 wt% and Mg# of orthopyroxene (Opx) in serpentinized harzburgites. Fields of Alpine-type peridotites and forearc peridotites compiled from literature by Khedr and Arai (2016, 2017), whereas thermally metamorphosed Opx in serpentinites (Khedr and Arai, 2012 and references therein) was used for comparison. Forearc, back-arc and abyssal peridotites fields in panel (**d**) compiled by Lian et al. (2019). (**e**) Spinel Cr# versus orthopyroxene $Al_2O_3 + Cr_2O_3$ (wt%) of the studied serpentinized peridotites. Abyssal and forearc peridotites are from Bonatti and Michael (1989) and Parkinson et al. (2003). (**f**) NiO vs. Cr_2O_3 (wt%) for analyzed serpentine minerals. Fields of serpentine after olivine and Opx are after Kodolányi et al. (2012).

Y_{Al} (0.30–0.45) and Y_{Fe} (<0.05) (Supplement 2).

Chromian spinel in Korab Kansi talc carbonates has the highest Cr# (0.74 on average) and lowest Mg# (0.1 on average) of our samples, reflecting intense alteration to form ferrritchromite (Fig. 6f). Most Cr-spinels in Korab Kansi prograde dunites are altered to ferritchromite (Fig. 6a; Supplement 2) with minor magnetite. This altered spinel composition is excluded from our petrogenetic and tectonic interpretations. Ferritchromite has higher NiO content (0.77–1.16 wt%), Y_{Fe} (0.64–0.86) and lower Y_{Al} (0.008–0.03), Y_{cr} (0.13–0.33) and Mg# (0.17–0.3) compared to fresh Cr-spinel (Table 2; Supplement 2). Magnetite is characterized by higher average Y_{Fe} (1.0) and NiO contents (1.26 wt%) than ferritchromite. Magnetite in talc-carbonate rocks has higher NiO (1.56–1.67 wt%) and lower FeO contents (77.6–78.5 wt%) than those of magnetite in harzburgites and dunites.

6. In-situ trace-element analyses

Trace element compositions of primary minerals (e.g. Cpx, Opx, olivine and spinel) can help constrain the origin and tectonic setting of mantle peridotites as well as mantle metasomatism (Scambelluri et al., 2006; Khedr et al., 2010, 2014). Opx in Abu Dahr and Korab Kansi harzburgites is depleted in light rare earth elements (LREEs, Ce-Sm), which are mostly below detection limits (Fig. 7a). Chondrite (C1)-normalized REEs of Opx show spoon-shaped patterns with high HREE/LREE [$(Lu/La)_N$ = 7–22.5] and HREE/MREE [$(Lu/Tb)_N$ = 1.47–31] (Fig. 7a; Supplement 3), similar to Opx in SSZ peridotites of Tonga (Birner et al., 2017) and SW Turkey (Aldanmaz, 2012). Primitive mantle (PM)-normalized trace element patterns of Opx exhibit positive spikes for U, Nb, Pb and Hf, and resemble those of Opx in SSZ peridotites of Tonga and SW Turkey (Fig. 7b). The investigated Opx in harzburgites is enriched in B, Li, Sc, V, Cr, Cs, Co, Ni, Zn and Ga, respectively (Fig. 7b).
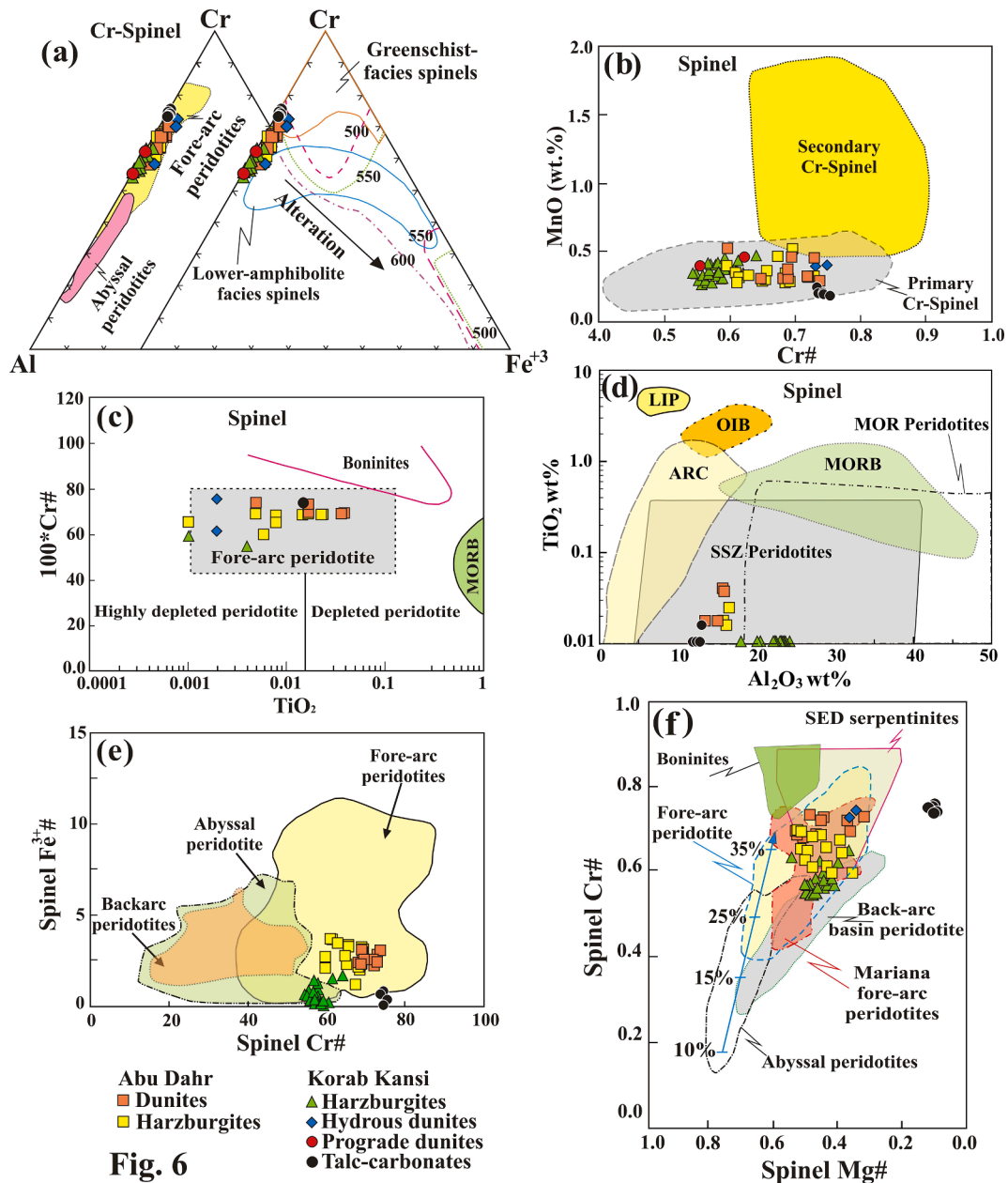
Fig. 6. (a) Cr–Al–Fe^{3+} ternary diagram (Barnes, 2000) showing spinel composition to distinguish between abyssal and forearc peridotites. Fields of forearc peridotite (Ishii et al., 1992), abyssal peridotite (Dick and Bullen, 1984) and Cr-spinel metamorphic facies (Evans and Frost, 1975; Barnes and Roeder, 2001) are shown for comparison. The stability fields of chromite and magnetite are after Sack and Ghiorso, 1991. (b) MnO versus Cr# for chromian spinel to distinguish between primary and secondary types. Fields of primary and secondary chromian spinel are after Khedr and Arai (2017). (c) Cr# versus TiO_2 diagram of chromian spinel. Fields of boninites, forearc peridotites and highly depleted to depleted peridotites are after Dick and Bullen (1984), Arai (1992), and Jan and Windley (1990). (d) TiO_2 versus Al_2O_3 discrimination diagram for chromian spinel, where fields of spinels in arc volcanics (Arc), ocean island basalt (OIB), mid-ocean ridge basalt (MORB), mid-ocean ridge peridotites and supra-subduction zone (SSZ) peridotites are after Kamenetsky et al. (2001). (e) Fe^{3+}# versus Cr# of examined chromian spinels. Forearc, back-arc and abyssal peridotites fields are compiled by Lian et al. (2019). (f) Cr# versus Mg# for chromian spinel. The trend of partial melting degrees is after Hirose and Kawamoto (1995). Fields of chromian spinel in forearc peridotites (Ishii et al., 1992), boninites (Barnes and Roeder, 2001), abyssal peridotites (Dick and Bullen, 1984), back-arc basin peridotites (Stern et al., 2004), Mariana forearc peridotites (Ohara and Ishii, 1998), SED peridotites (Farahat et al., 2011) and Gerf serpentinites (Abdel-Karim et al., 2016) are shown for comparison.

Its enrichment in mobile elements (B, Li and Cs) may result from subducted slab-derived fluids (Khedr et al., 2010). Opx is the main host of Sc, V, Co and Cr in harzburgites (Fig. 7b). Opx is depleted in high field strength elements (HFSE: Nb, Ta, Zr, Ti), Y and LREE (<0.2 times PM; Fig. 7b).

Korab Kansi tremolite contains more rare earth elements (ΣREE = 2.03–5.39 ppm; Supplement 3) than do coexisting minerals (Fig. 7c). C1-normalized REE patterns are characterized by steeply inclined slopes from La to Sm (($La/Sm)_N$ = 2.86–4.14) with a variable LREE enrichment

relative to MREE (La_N/Gd_N = 1.25–19.33) (Fig. 7c). PM-normalized trace-element patterns of tremolite are enriched in fluid-mobile elements (B, Li, Cs, Pb, Rb, Th and U), Sc, V and Cr, while Nb and Ti are highly depleted relative to adjacent elements (Fig. 7d). The U-shaped REE (Fig. 7c) and spider patterns (Fig. 7d) of Korab Kansi tremolite are similar to those of tremolites in forearc hydrous peridotites, such as those of the Ulten Zone in Italy (Marocchi et al., 2007).

Analyzed Abu Dahr and Korab Kansi olivines are depleted in REE (<0.05 times C1), and most trace and REEs are below detection limits
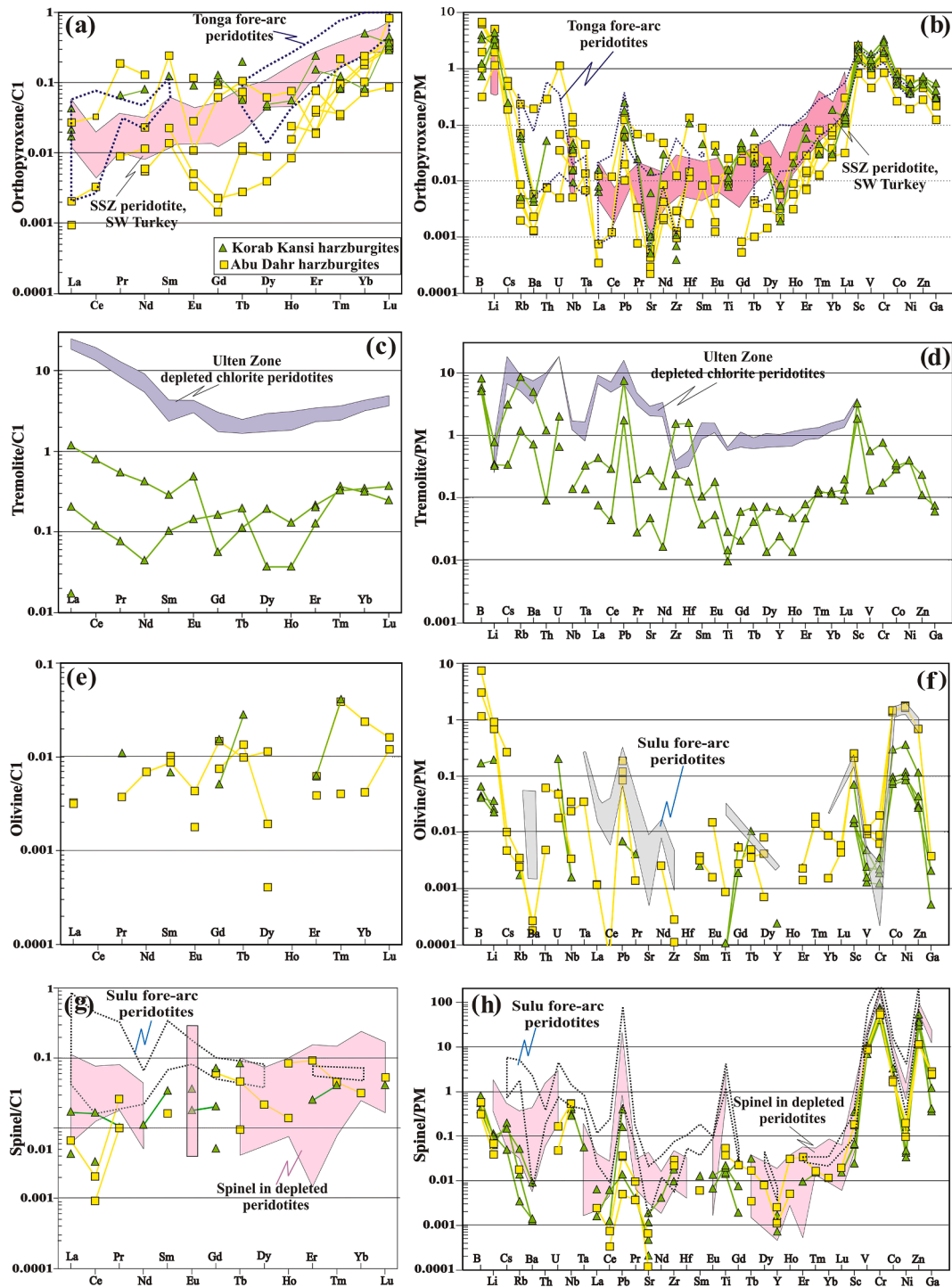
Fig. 7. In-situ trace and rare earth elements of Abu Dahr and Korab Kansi orthopyroxene, tremolite, olivine and spinel. (**a, c, e, g**) Chondrite (C1)-normalized REEs patterns. (**b, d, f, h**) Primitive mantle (PM)-normalized trace-elements patterns. C1 and PM normalized values are after McDonough and Sun (1995). Fields of Opx in SSZ peridotites from both Tonga (Birner et al., 2007) and SW Turkey (Aldanmaz, 2012), tremolite in depleted peridotites from Ulten Zone, Italy (Marocchi et al., 2007) and spinels in Sulu forearc peridotites (Xie et al., 2021) and depleted peridotites from SW Greenland (Szilas et al., 2018) are shown for comparison.

(Fig. 7e). PM-normalized trace-element patterns of olivine show positive anomalies for most fluid mobile elements (B, Li, U, Pb), Sc, Co and Ni, but negative anomalies for Ba, Y, Zr, V, Cr, Ga and REE (Fig. 7f). Investigated olivines contain B and Li, similar to mantle olivine (Khedr et al., 2010). Co, Ni and Zn are preferentially incorporated in olivines as they have charge and ionic radii like that of Mg (De Hoog et al., 2010). Abu Dahr olivine is enriched in most trace elements relative to Korab Kansi olivine (Fig. 7f). The relative enrichment of Abu Dahr olivine in B,

Li and Pb (Fig. 7f) may indicate that Abu Dahr peridotites were more strongly affected by slab-derived fluids

Chromian spinel is very depleted in REE (ΣREE = 0.008–0.034 ppm; Supplement 3). CI-normalized REE patterns of Cr-spinel scatter, and are highly depleted (<0.1 times CI) (Fig. 7g). Chromian spinel prefers V, Cr and Zn (7–75 times CI) relative to associated silicate minerals (Fig. 7h). It also displays positive spikes for B, Cs, Pb, and HFSE (e.g. Nb, Zr, Ti) but is poor in Ba, Sr, Ce, Gd and Y (Fig. 7h).

7. Whole-rock chemistry

Loss on ignition (LOI) of analyzed ultramafic rocks ranges from 7.74 to 14.43 wt%, reflecting variable serpentinization (Table 3). Highly serpentinized Korab Kansi dunites show higher LOI values (12.26–14.43 wt%) than less serpentinized harzburgites (7.74–11.25 wt%) (Table 3), suggesting more serpentinization of olivine than orthopyroxene. Mg# of Abu Dahr and Korab Kansi serpentinized peridotites shows a narrow range (0.9–0.92), similar to that of other SED serpentinites (Mg#: 0.9–0.93; Khedr and Arai, 2013; Azer et al., 2013; Abdel-Karim et al., 2016). Peridotite Mg# is consistent with its olivine Mg# (0.9–0.94) and Opx Mg# (0.9–0.93) (Supplement 2). Analyzed serpentinized peridotites are greatly depleted in magmaphile major elements such as TiO_2 (0.01–0.013 wt%), Al_2O_3 (0.27–0.53 wt%) and CaO (0.24–0.48 wt%) relative to primitive mantle (TiO_2, 0.2 wt%; Al_2O_3, 4.49 wt% and CaO, 3.65 wt%; McDonough and Sun, 1995). Serpentinized harzburgites contain more SiO_2, CaO, Al_2O_3 and Cr_2O_3 than serpentinized dunites (Table 3). Both have high abundances of compatible elements such as Cr (2193–3339 ppm) and Ni (2299–2656 ppm) with little Co (99–115 ppm), Zn (33–55 ppm) and V (24–33 ppm) (Table 3).

Serpentinized harzburgites and dunites are poor in REE (ΣREE: 0.02–0.15 ppm; Table 3). C1-normalized REEs of Korab Kansi serpentinized peridotites (McDonough and Sun, 1995) show U-shaped patterns (Fig. 9a) with depleted MREE relative to LREE [$(La/Gd)_N$: 1–4] and HREE [$(Lu/Gd)_N$: 2.67–12]. They exhibit spikes for B (>10 times PM), Th, Pb, Ta, Sr, Sc and Ti (Fig. 9b). Generally, the studied peridotites are depleted in HFSE (Nb, Zr, Ti) relative to fluid mobile elements (B, Th, Pb, Sr, Rb, Ba and Li) and REEs [e.g. $(B/Zr)_N$: 1046–2137; $(B/Lu)_N$: 128.2–712.3] (Fig. 9b).

8. Discussion

Below we discuss four implications resulting our study: 1) Temperature and oxygen fugacity (fO_2) conditions of SED ophiolitic peridotites; 2) Petrogenesis of SED ophiolitic peridotites, including equilibrium melt composition, partial melting extent and peridotite depletion; 3) Geodynamic implications of Arabian-Nubian Shield ophiolitic peridotites; and 4) Chemical changes related to serpentinization and metamorphism. These four topics are explored further below.

8.1. Temperature and oxygen fugacity (fO₂) conditions of SED ophiolitic peridotites

Oxygen fugacity (fO_2) was calculated for coexisting spinel and olivine pairs (Table 4) based on the fayalite-magnetite-quartz (FMQ) buffer (Ballhaus et al., 1991). The investigated olivine-spinel pairs (Table 4; Fig. 11a) are used to calculate the oxygen fugacity at which our mantle-derived peridotites equilibrated. The oxygen fugacity (Δlog fO_2) is FMQ + 1.7 to FMQ + 2.42 and FMQ + 0.26 to FMQ + 2.58 for Abu Dahr and Korab Kansi peridotites, respectively, at 1.5 GPa (Table 4; Fig. 11a) (Ballhaus et al., 1991). The wide range of Δlog fO_2 of SED peridotites suggest variable oxidation states and slab-derived fluids. Korab Kansi hydrous dunites are more oxidized (Δlog fO_2: FMQ + 1.86 – FMQ + 2.58) than harzburgites (Δlog fO_2: FMQ + 0.26 – FMQ + 1.14) (Table 4; Fig. 11a). Calculated fO_2 of SED peridotites is compared with that of continental peridotites (Parkinson and Pearce, 1998), arc peridotites (Parkinson and Arculus, 1999; Rolland et al., 2002), abyssal peridotites (Dick and Bullen, 1984; Parkinson and Pearce, 1998) and forearc peridotites (Ishii et al., 1992; Parkinson and Pearce, 1998) (Fig. 11a). The Δlog fO_2 values of Korab Kansi peridotites plot in the field of forearc peridotites, whereas those of Abu Dahr peridotites are higher and plot in the field of arc peridotites (Fig. 11a). Both indicate a

Table 4
Melt calculations, *fO2* and crystallization temperature for Abu Dahr and Korab Kansi mantle peridotites.

Area	Lithology	Sample No	Al₂O₃ (spinel)	Al₂O₃ (melt)	FeO/MgO	ln (FeO/MgO) spinel	YAl spinel	YFe³⁺ spinel	ln FeO/MgO melt	Cr#	Δlog (fO₂) FMQ (Ballhaus et al., 1991)	T °C (Ballhaus et al., 1991)	T °C (Brey and Kohler, 1990)
Abu Dahr	Harzburgites	Rh.75r	19.82	13.73	2.30	0.833	0.371	0.119	0.736	0.62	2.15	748.99	1203.70
	Harzburgites	Rh.75r	20.20	13.84	2.30	0.831	0.376	0.121	0.739	0.61	2.27	774.47	
	Harzburgites	Rh.75r	17.91	13.16	1.65	0.502	0.333	0.129	0.366	0.66	2.05	905.81	
	Harzburgites	Rh.73r	17.62	13.08	2.26	0.814	0.331	0.111	0.678	0.66	2.00	764.45	1099.56
	Harzburgites	Rh.73r	19.31	13.58	1.75	0.559	0.358	0.129	0.450	0.63	2.42	852.34	
	Harzburgites	Rh78r	16.14	12.61	2.07	0.727	0.303	0.082	0.566	0.69	1.86	757.36	
	Harzburgites	Rh.72r	16.33	12.67	1.91	0.648	0.307	0.082	0.492	0.69	2.28	781.29	912.65
	Harzburgites	Rh.72r	16.56	12.75	1.72	0.542	0.309	0.083	0.390	0.68	1.78	818.24	911.80
	Harzburgites	Rh.72r	16.78	12.81	1.70	0.532	0.311	0.092	0.379	0.68	2.11	828.30	932.29
Average			**17.85**	**13.14**	**1.96**	**0.67**	**0.33**	**0.11**	**0.53**	**0.66**	**2.10**	**803.47**	**1012.00**
	Dunites	Rh.74r	13.28	11.63	1.85	0.615	0.254	0.111	0.397	0.74	1.70	873.01	
	Dunites	Rh82r	15.94	12.55	1.99	0.688	0.304	0.082	0.528	0.69	1.84	772.42	
Average			**14.61**	**12.09**	**1.92**	**0.65**	**0.28**	**0.10**	**0.46**	**0.71**	**1.77**	**822.71**	
Korab Kansi													
	Harzburgites	Sn18r	23.57	14.75	2.33	0.844	0.379	0.046	0.840	0.62	0.97	627.06	
	Harzburgites	Sn25r	24.84	15.07	1.98	0.683	0.453	0.019	0.694	0.54	0.26	633.71	973.30
	Harzburgites	Sn25r	24.30	14.93	1.86	0.621	0.446	0.020	0.625	0.55	0.85	658.60	1027.96
	Harzburgites	Sn-36r	22.28	14.41	2.49	0.912	0.417	0.040	0.881	0.58	0.35	612.14	1115.52
	Harzburgites	Sn-36r	22.62	14.50	2.67	0.984	0.425	0.045	0.959	0.57	0.67	602.84	1108.10
	Harzburgites	Sn-32r											968.01
	Harzburgites	Sn-32r											1039.83
	Harzburgites	Sn-32r											1062.18
Average			**23.52**	**14.73**	**2.27**	**0.81**	**0.42**	**0.03**	**0.80**	**0.57**	**0.62**	**626.87**	**1042.13**
	hydrous dunites	Sn38r	12.74	11.44	3.64	1.291	0.255	0.129	1.064	0.73	1.86	679.84	
	hydrous dunites	Sn38r	11.99	11.15	3.84	1.345	0.241	0.104	1.108	0.75	1.96	647.14	
	hydrous dunites	Sn38r	19.66	13.68	2.70	0.994	0.372	0.144	0.891	0.61	2.58	706.39	
Average			**14.80**	**12.09**	**3.39**	**1.21**	**0.29**	**0.13**	**1.02**	**0.70**	**2.13**	**677.79**	

convergent margin setting. The fO_2 can also be estimated by using the bulk-rock V content of these peridotites because vanadium is strongly controlled by fO_2 during partial melting (Pearce and Parkinson, 1993). On the V versus Yb diagram, the investigated peridotites scatter between QFM and QFM + 1, indicating high fO_2 (Fig. 12d).

The temperature calculated using orthopyroxene (Ca contents) thermometer of Brey and Kohler (1990), giving on average 1012 ± 80 °C and 1042 ± 73 °C for Abu Dahr and Korab Kansi harzburgites, respectively (Table 4). This is considered as crystallization temperature of Opx that is higher than equilibrium temperature calculated from coexisting mineral pairs. Equilibrium temperatures can be calculated from co-existing spinel and olivine compositions (Table 4) (Ballhaus et al., 1990, 1991; Evans and Frost, 1975; Sack and Ghiorso, 1991). The partition coefficient KD^{Mg-Fe} between olivine and spinel is essentially a function of temperature at a given spinel Ycr ratio [$(Cr/(Cr + Al + Fe^{+3})$] (Evans and Frost, 1975). Primary chromian spinel coexisting with olivine has Cr# (0.6–0.74), Ycr (0.58–0.72) and ln K_D (2.14–2.52) for Abu Dahr peridotites and Cr# (0.54–0.75), Ycr (0.54–0.72) and ln K_D (2.4–3.14) for Korab Kansi peridotites (Table 4; Supplement 2). These indicate subsolidus equilibrium temperatures ranging from 750 to 900 °C and 610–710 °C for Abu Dahr and Korab Kansi peridotites, respectively (Evans and Frost, 1975; Ballhaus et al., 1990) (Table 4; Fig. 11b). Low equilibrium temperatures of these rocks are consistent with an origin as supra-subduction zone peridotites and may reflect the addition of water from the subducted slab (Parkinson and Pearce, 1998). Finally, the occurrence of antigorite with interpenetrating textures (Supplement 1) suggest temperatures of 400–600 °C (Evans, 2010) for Korab Kansi serpentinites.

8.2. Petrogenesis of SED ophiolitic peridotites

8.2.1. Evidence of pristine compositions of mantle-derived mineral phases

Serpentine, talc, tremolite, magnetite, ferritchromite and carbonates are secondary minerals (Fig. 4a, e-h) in the studied serpentinized peridotites. However, primary minerals (olivine, Opx and Cr-spinel) survived (Fig. 4a-d, i-j). It is well known that primary minerals in mantle-derived rocks change in compositions during cooling and decompression (e.g., Arai, 1980; Khedr and Arai, 2013). Mg and Fe exchange between olivine, pyroxenes and spinel during re-equilibration and compositions of pyroxenes (Ca, Cr, Al) and spinel (Fe, Mg) will be modified during cooling. changing mineral compositions depends on a number of things, including mineral proportions, exsolution structures, rate (slow vs fast) of cooling and re-equilibrium temperatures (e.g., Arai, 1980; Khedr and Arai, 2013) and is likely to also affect trace elements. Primary minerals in Korab Kansi and Abu Dahr peridotites with primary textures (Fig. 4; Supplement 1) show slight changes in chemical compositions as a result of re-equilibration during cooling. These compositions can be treated as primary and still plot within a specific field based on characteristics described below.

In peridotites, olivine Mg# is nearly constant because of the high abundance of MgO; so olivine Mg# depends on olivine proportions. The investigated peridotite Mg# (0.90–0.92) is consistent with its olivine Mg# (0.9–0.94) (Tables 1, 3) due to high abundance of olivine and low spinel proportions, suggesting little Fe–Mg exchange during cooling. Olivines in Korab Kansi and Abu Dahr peridotites show primary textures (Fig. 4a-d) without opaque inclusions (Fig. 4c) and have pristine compositions (Fo$_{90.6-92.2}$; NiO, 0.39 wt%; MnO, 0.13 wt%) similar to primary mantle olivines (Arai, 1980; Takahashi et al., 1987) (Fig. 5a, b) and primary olivines in Oman ophiolitic harzburgites (Khedr et al., 2014). In contrast, secondary and metamorphic olivines are poor in NiO (<0. 2 wt%) and MnO (<0. 01 wt%), and either have very high Fo (>95) or very low Fo contents (<0.86) (Khedr and Arai, 2012 and references therein). These olivines are also highly pitted with opaque inclusions (Khedr and Arai, 2012), which is not seen in our study (Fig. 4). Laminated (Fig. 4a, d) and coarse prismatic Opxs (Fig. 4a) show equilibrated textures with olivine and vermicular Cr-spinel, similar to

textures and minerals in Oman fresh peridotites (Khedr et al., 2014). Opx compositions (Table 1; Supplement 2) resemble primary mantle Opx in peridotites (Fig. 5c). The high CaO (0.6–3.0 wt%) content of Opx reflects minor exsolved Cpx lamella during subsolidus unmixing. In addition, Tschermak's components (Al and Cr contents) of Opx are also lowered by exsolution of spinel components, which is not seen in our study. Mg# of peridotite Opx is also unchanged because the Mg–Fe distribution coefficient with olivine is almost unity. Consequently, our peridotite Mg# (0.90–0.93) is consistent with its Opx Mg# (0.9–0.93) (Tables 1, 3). SED Opx Al$_2$O$_3$, Cr$_2$O$_3$ and CaO contents are higher than those (<0.5 wt%) of Opx in Happo-O'ne forearc metaperidotites, which suffered from low-T subsolidus modification (Khedr and Arai, 2010). Therefore, Abu Dahr and Korab Kansi Opx has pristine composition and was not seriously modified by subsolidus re-equilibration.

Abu Dahr and Korab Kansi Cr-spinels occur as primary minerals together with olivine and Opx (Fig. 4a-d, f, i) in spinel-facies mantle peridotites. They are vermicular (Fig. 4d), homogenous (Fig. 4c, j) and red in color similar to mantle spinels (Fig. 4a-d, i). These primary Cr-spinels have low MnO (0.18–0.52 wt%) (Fig. 6b), TiO$_2$ (<0.05 wt%) (Fig. 6c, d), and Y$_{Fe}$ (<0.05) but high Fe^{2+}/Fe^{3+} (>5) (Supplement 2), consistent with mantle spinel compositions (Kamenetsky et al., 2001; Khedr and Arai, 2017). Low contents of spinel MnO (<0.52 wt%; Fig. 6b), Fe$_2$O$_3$ (<3.0 wt%), Fe$_2$O$_3$/FeO (<0.16) and Fe^{+3}/(Fe^{+3} + Al + Cr) ratio (0.021 on average) (Supplement 2) indicate primary compositions and little alteration. Altered Cr-spinel has elevated, Mn, Fe^{3+} and Fe^{2+} values relative to Al and Mg (Fig. 6b; Supplement 2). Investigated spinel compositions plot in the space of primary forearc peridotite spinel and far away from spinel fields of greenschist facies and low-amphibolite facies (Fig. 6a). They do not lie along an alteration trend (Fig. 6a) or plot in the secondary spinel field (Fig. 6b). Spinel Cr/Al and Mg/Fe may exchange with olivine during subsolidus modification (Arai, 1980; 1994a), but this is not a serious concern based on low values of Cr/Al (1.2–2.8) and Mg/Fe (0.86–2.1) and trend of Cr# versus Mg# for our peridotites (Fig. 6f; Supplement 2). Spinel Mg# value is not very low at high Cr# (Fig. 6f) due to little Fe–Mg exchange with olivine. Examined spinels have pristine compositions and its REE and trace-element patterns resemble those of primary spinels in depleted peridotites (Fig. 7g, h) (Szilas et al., 2018; Xie et al., 2021). Excellent preservation of primary spinels may reflect fast cooling of peridotites. Consequently, we conclude that most of the investigated chromian spinels are primary and serve as an important petrogenetic (magmatic) indicators of SED peridotites.

8.2.2. Equilibrium melt compositions

Compositions of melts in equilibrium with the investigated peridotites can be constrained from primary chromian spinel compositions (Tables 2, 4) (Maurel and Maurel, 1982; Kamenetsky et al., 2001). Equilibrium melt composition are controlled by the extent of partial melting and peridotite composition, including interactions with slab-derived fluids (e.g. Arai, 1997; Khedr and Arai, 2013, 2017). Maurel and Maurel (1982) calculated parental-melt compositions based on spinel Al$_2$O$_3$, FeO, MgO and TiO$_2$ contents. Chromian spinel, olivine and pyroxenes are in equilibrium with some primitive melts, as confirmed by melting experiments (Jaques and Green, 1980; Matsukage and Kubo, 2003). For residual spinel peridotites, extracted magmas should have been in equilibrium with residual peridotites and their spinel compositions. Residual peridotite minerals should have the same compositions as the first phases precipitated from the extracted magmas (Arai, 1994b).

Melt in equilibrium with chromian spinel in Abu Dahr dunites is low in Al$_2$O$_3$ (11.6–12.8 wt%), but has the same FeO/MgO (1.3–3.0) and TiO$_2$ (0.015–0.084 wt%) contents as melts in equilibrium with harzburgite spinels (Al$_2$O$_3$, 12.5–14.0 wt%)(Table 4; Supplement 2). These equilibrium melt compositions resemble Phanerozoic boninitic melts from Chichijima, Japan (Hickey and Frey, 1982) (Supplement 2) and plot in the boninite field of Barnes and Roeder (2001) (Fig. 11d). The

high Cr# (0.68 on average) of Abu Dahr peridotite Cr-spinels is inter-preted to reflect primitive high-Mg melts (e.g. boninite or Mg-rich tholeiite) generated in a forearc setting (Beccaluva et al., 2004). The melt in equilibrium with chromian spinel in Korab Kansi hydrous du-nites is also low in Al_2O_3 (11.2–13.7 wt%), with similar FeO/MgO (1.8–3.0) and TiO_2 (0.004–0.013 wt%) contents to equilibrium melt compositions (Al_2O_3, 13.8–15.0 wt%) of harzburgite spinels (Table 4; Supplement 2). This is similar to Ti-poor island-arc tholeiitic (IAT) to boninitic melts from the Kizildag ophiolite, Turkey (Dilek and Thy, 2009) (Supplement 1). Such melts result from partial melting of mantle peridotites, most likely during the subduction initiation or an infant arc stage.

8.2.3. Peridotite partial melting and depletion

Low concentrations of Al_2O_3, CaO and TiO_2 in the studied peridotites (Table 3) relative to primitive mantle suggest high degrees of partial melting (Hellebrand et al., 2001; Takazawa et al., 2003; Khedr et al., 2014). This agrees with whole-rock MgO/SiO_2 (0.94–1.06) and Al_2O_3/SiO_2 (0.007–0.013) ratios that plot between forearc and abyssal peri-dotites, at the refractory end of the melting residue trend (Table 3; Fig. 8d). These ratios are very close to those of highly depleted harz-burgite ($MgO/SiO_2 \sim 1.1$; $Al_2O_3/SiO_2 \sim 0.01$; Niu, 2004; Fig. 8d) and indicate that the mantle protolith suffered from extensive partial melting (Snow and Dick, 1995; Paulick et al., 2006). Examined peri-dotites are enriched in compatible elements such as Cr (up to 3339 ppm) and Ni (up to 2656 ppm) with lower concentrations of Co (115 ppm), Zn (55 ppm) and V (33 ppm), reflecting the highly depleted nature of the oceanic mantle beneath this part of the ANS (Table 3).

The extent of mantle peridotite partial melting can be estimated using their mineral and whole-rock compositions (Hellebrand et al., 2001; Niu, 2004; Uysal et al., 2012). Very low HREE concentration of the studied peridotites (Fig. 12a) relative to depleted MORB mantle (DMM; Workman and Hart, 2005) is interpreted to result from extensive partial melting of the mantle. HREE abundances of the investigated serpentinized peridotites compared with DMM melting curves of the spinel stability field (De Hoog et al., 2009) indicate ~25% melting (Fig. 12a). This is supported by variations of Al_2O_3 versus MgO, which give similar degrees of melt extraction (Fig. 12b). Moreover, Yb (ppm) versus Sc and V (ppm) diagrams also indicate ~25% melting (Fig. 12c, d). Chondrite-normalized REEs of the investigated peridotites show U-shaped patterns (Fig. 9a), indicating that these are residues that were enriched in LREE as a result of metasomatism by slab fluids (e.g., Niu, 2004). These are similar to U-shaped REE patterns of highly depleted SSZ mantle peridotites such as those of South Sandwich, Izu-Bonin-Mariana and Yushigou forearc peridotites (Pearce et al., 2000; Parkin-son and Pearce, 1998; Song et al., 2009).

Spinel compositions are also useful for estimating extent of partial melting (Dick and Bullen, 1984; Arai, 1994a; Hellebrand et al., 2001; Khedr et al., 2010, 2014). Spinels in Korab Kansi and Abu Dahr ser-pentinized peridotites plot within the olivine-spinel mantle array (OSMA) (Arai, 1994a) and suggest 25–40% partial melting (Fig. 11c), similar to 15–40% partial melting estimated for SSZ peridotites (Par-kinson and Pearce, 1998; Pearce et al., 2000). Abu Dahr harzburgites and dunites were generated after 30–35 % and 35–40 % melting, respectively. In contrast, Korab Kansi harzburgites and dunites were generated after 25–30 % and 30–40 % melting, respectively (Arai, 1994a; Pearce et al., 2000) (Fig. 11c).

The high degree of partial melting (>25%) of the examined ser-pentinized peridotites is consistent with high olivine Fo (90.6–92.2; Table 1; Fig. 5a) and the absence of Cpx, which is exhausted at ~20% partial melting (Jennings and Holland, 2015). This absence of Cpx in-dicates that SED peridotites were exhausted by extensive partial melting
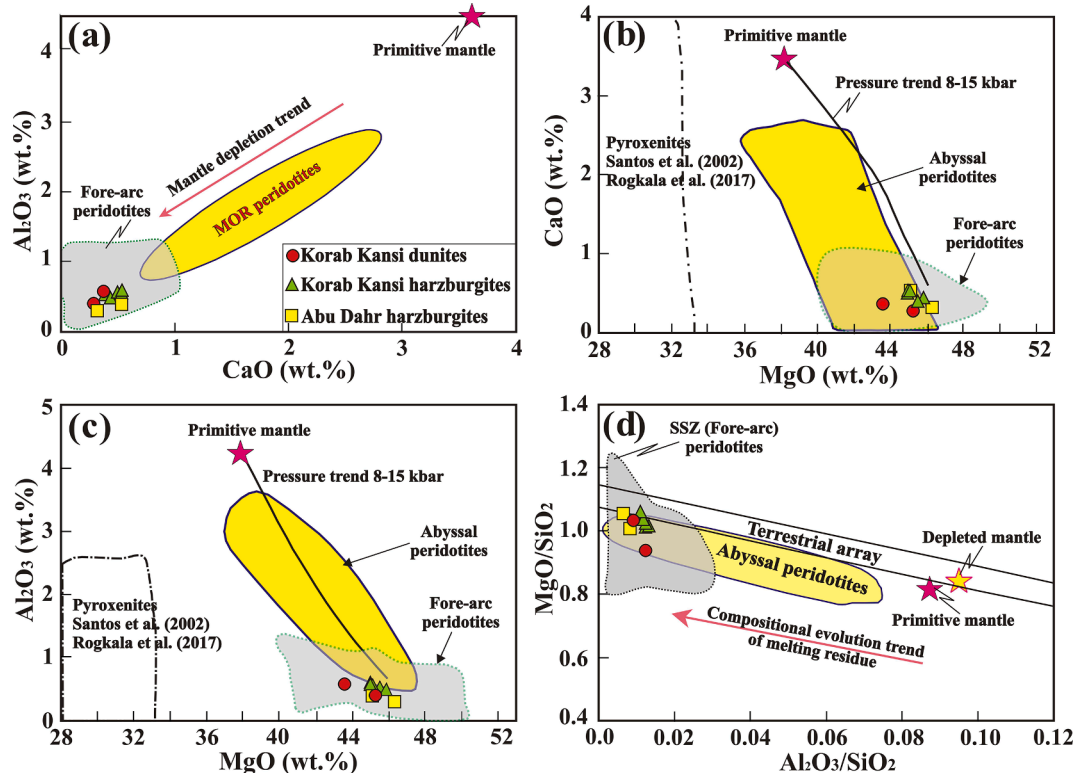

Fig. 8. Whole-rock chemistry of Abu Dahr and Korab Kansi serpentinized peridotites. (**a**) CaO versus Al_2O_3 diagram showing Abu Dahr and Korab Kansi serpen-tinized peridotites compared with MOR- and forearc peridotites (Ishii et al., 1992). Primitive mantle values are after McDonough and Sun (1995). (**b, c**) MgO versus both CaO and Al_2O_3. Fields of forearc and abyssal peridotites and pressure trends are compiled by Lian et al. (2019). Field of ophiolitic pyroxenites is after Santos et al. (2002) and Rogkala et al. (2017). (**d**) Al_2O_3/SiO_2 versus MgO/SiO_2 diagram. Abyssal and forearc peridotite fields are after Niu (2004), Pearce et al. (2000) and Parkinson and Pearce (1998). The terrestrial array field is after Jagoutz et al. (1979) and Hart and Zindler (1986).
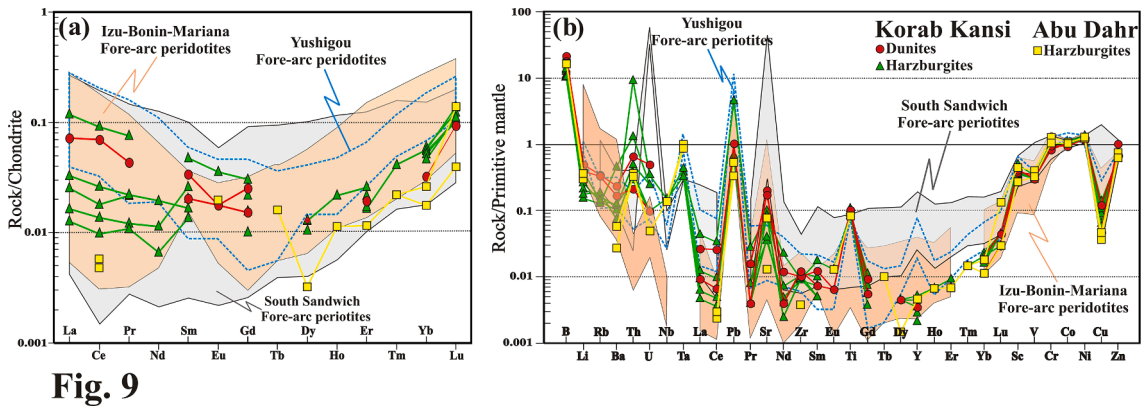
Fig. 9. Trace and rare earth elements (REE) of Korab Kansi and Abu Dahr serpentinized peridotites. (**a**) Chondrite (C1)-normalized REEs patterns. (**b**) Primitive mantle (PM)- normalized multielement patterns. The C1 and PM normalized values are from McDonough and Sun (1995). Fields of South Sandwich forearc (Pearce et al., 2000), Izu-Bonin-Mariana (Parkinson and Pearce, 1998) and Yushigou forearc peridotites (Song et al., 2009) are shown for comparison.
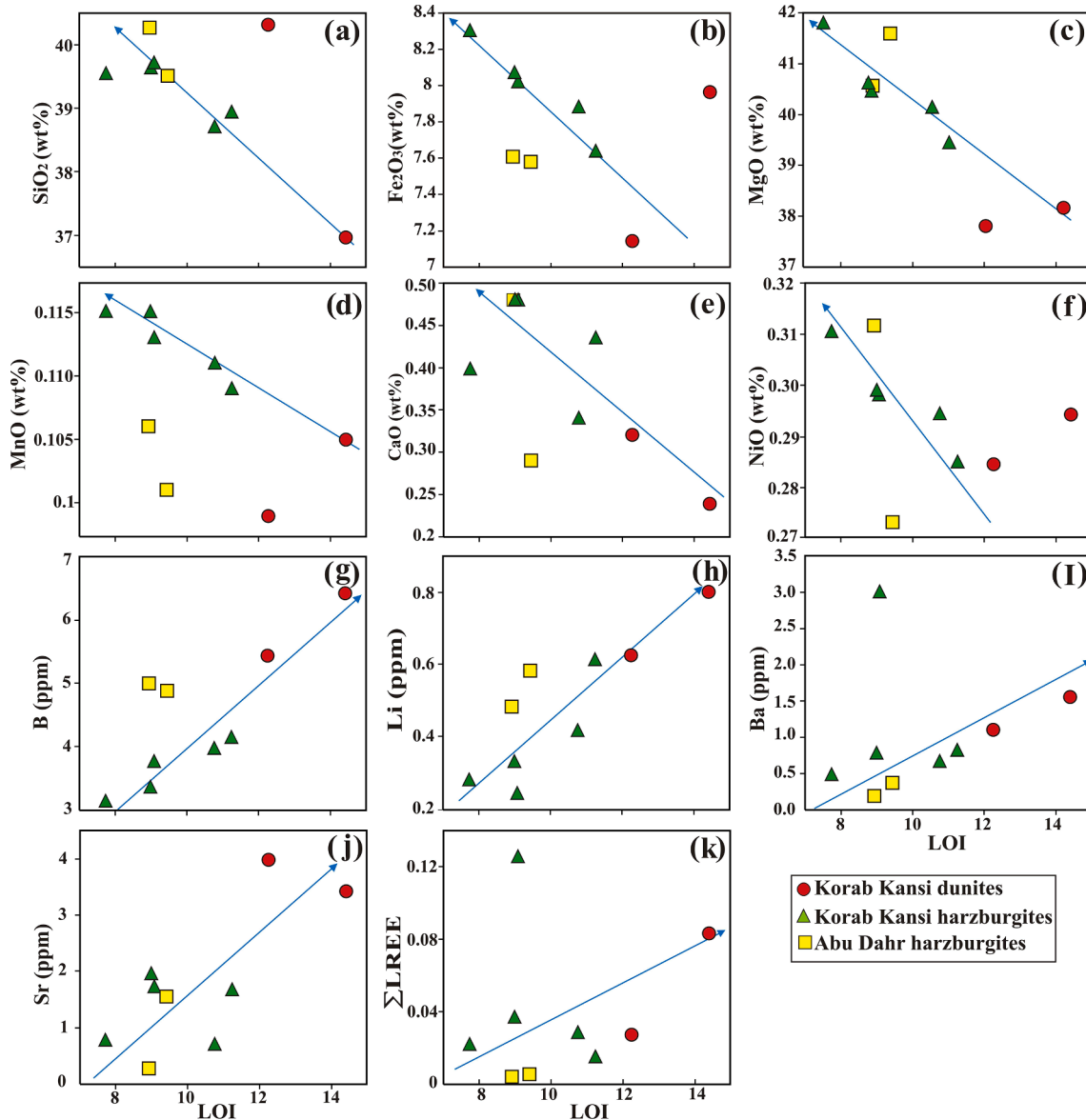

Fig. 10. Variation diagrams showing the relation between LOI and selected major, trace and rare earth elements for investigated serpentinized harzburgites and dunites.

(Khedr et al., 2010; Jennings and Holland, 2015), to the point of forming boninitic magmas. Some boninitic melts may have crystallized to form high-Cr chromitites and Opx veins in the serpentinized harzburgites (Fig. 3h). The absence of Cpx, high Fo contents of residual olivine and high chromian spinel Cr# (>0.53) indicate high degrees of partial melting and hydrous environments such as expected for a forearc setting. Abu Dahr and Korab Kansi serpentinized peridotites show similar high degrees of partial melting (~25–40%) with other SED forearc peridotites (Khedr and Arai, 2013, 2016; Ahmed, 2013; Abdel Halim et al., 2020). We think that the high degree of partial melting of the investigated peridotites was related to abundant slab-derived fluids that lowered the peridotite melting temperature (Grove et al., 2006) and consequently promotes partial melting. Finally, mineral chemistry and whole-rock analyses of the investigated SED peridotites reveal that these are residues after extensive partial melting.

8.3. Geodynamic implications of Arabian-Nubian Shield ophiolitic peridotites

ED ophiolitic peridotites provide key constraints for Neoproterozoic mantle geodynamic evolution beneath the Arabian-Nubian Shield (ANS). Partial melting variations (20–40% melting), the wide range of

oxidation state (Δlog fO_2, FMQ + 0.26– FMQ + 2.58) and variation of mantle fertility reflect changing tectonics.

ANS peridotites are suggested to have evolved in different tectonic environments, like mid-oceanic ridge (MOR) and supra-subduction zone (SSZ) settings (e.g. Zimmer et al., 1995; Stern et al., 2004; Azer and Khalil, 2005; Ahmed, 2013; Khedr and Arai, 2013, 2016, 2017). Field observations of Abu Dahr and Korab Kansi peridotites show that they are associated with island-arc metavolcanic rocks (Fig. 2). Moreover, the estimated ages (>741 Ma) (Kröner et al., 1992) for Korab Kansi peridotites and relative age > 744 Ma (Ali et al., 2015) of Abu Dahr peridotites are similar with ED arc volcanics age (720–770 Ma; Stern and Hedge, 1985). These features support a subduction-related environment for the studied peridotites.

Our geochemical results for Abu Dahr and Korab Kansi peridotites show that these are similar to forearc peridotites (Figs. 5–12). Analyzed serpentinized peridotites plot in the forearc peridotite field (Fig. 8a–c). They also have very low SiO_2/MgO and Al_2O_3/SiO_2 ratios, similar to SSZ forearc peridotites (Table 3; Fig. 8d). Their U-shaped REE patterns (Fig. 9a) and multi-element patterns with peaks at Sr and Pb are similar to forearc mantle peridotites from South Sandwich, Izu-Bonin-Mariana and Yushigou (China) (Parkinson and Pearce, 1998; Godard et al., 2000; Pearce et al., 2000; Song et al., 2009) (Fig. 9b). In addition, very
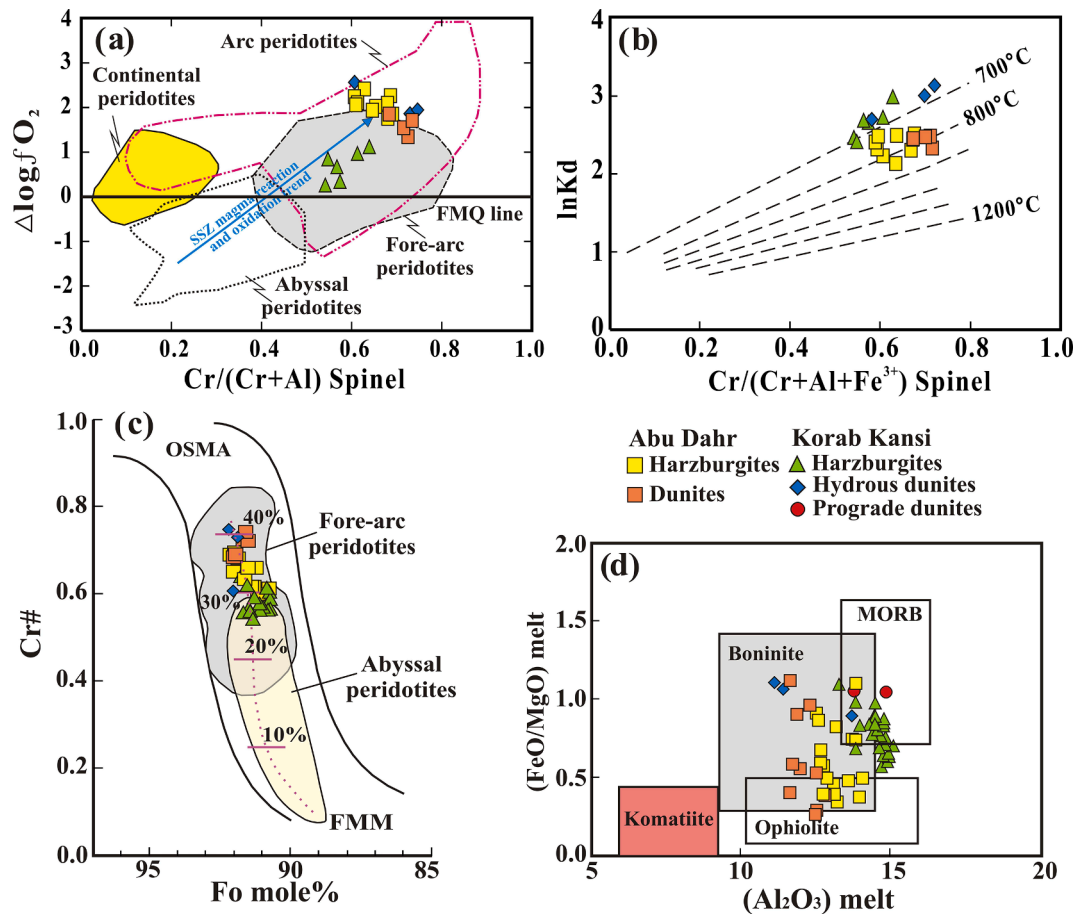

Fig. 11. Implications of peridotite mineral chemistry. (**a**) Oxygen fugacity (ΔlogfO_2) versus spinel Cr# of Abu Dahr and Korab Kansi serpentinized harzburgites and dunites based on fayalite-magnetite-quartz (FMQ) buffer (Ballhaus et al., 1991). Fields of arc peridotites (Parkinson and Arculus, 1999; Rolland et al., 2002), abyssal peridotites (Dick and Bullen, 1984; Parkinson and Pearce, 1998) and forearc peridotites (Ishii et al., 1992; Parkinson and Pearce, 1998) are shown for comparison. The continental peridotite field and the blue arrow show the trend for residual peridotites interacting with supra-subduction zone (SSZ) melts after Parkinson and Pearce (1998). (**b**) Olivine-spinel geothermometry of serpentinized peridotites based on InKd(=$X^{Olv}_{Mg}/X^{Olv}_{Fe}$. $X^{spl}_{Fe2+}/X^{spl}_{Mg}$) of olivine-spinel pairs versus Cr/(Cr + Al + Fe^{3+}) of chromian spinel. The 700 °C and 1200 °C isotherms are after Evans and Frost (1975). (**c**) Spinel Cr# versus olivine Fo (forsterite) showing partial melting% and tectonic settings. Fields of chromian spinel in forearc peridotites (Ishii et al., 1992; Parkinson and Pearce, 1998) and abyssal peridotites (Arai, 1994; Khedr et al., 2014) are used for comparison. OSMA (olivine–spinel mantle array) is the spinel peridotite restite trend (Arai, 1994). (**d**) (FeO/MgO)$_{melt}$ versus (Al$_2O_3$)$_{melt}$ of chromian spinel showing parental melt compositions. Fields of several tectonic settings are from Barnes and Roeder (2001). (For interpretation of the references to color in this figure legend, the reader is referred to the web version of this article.)
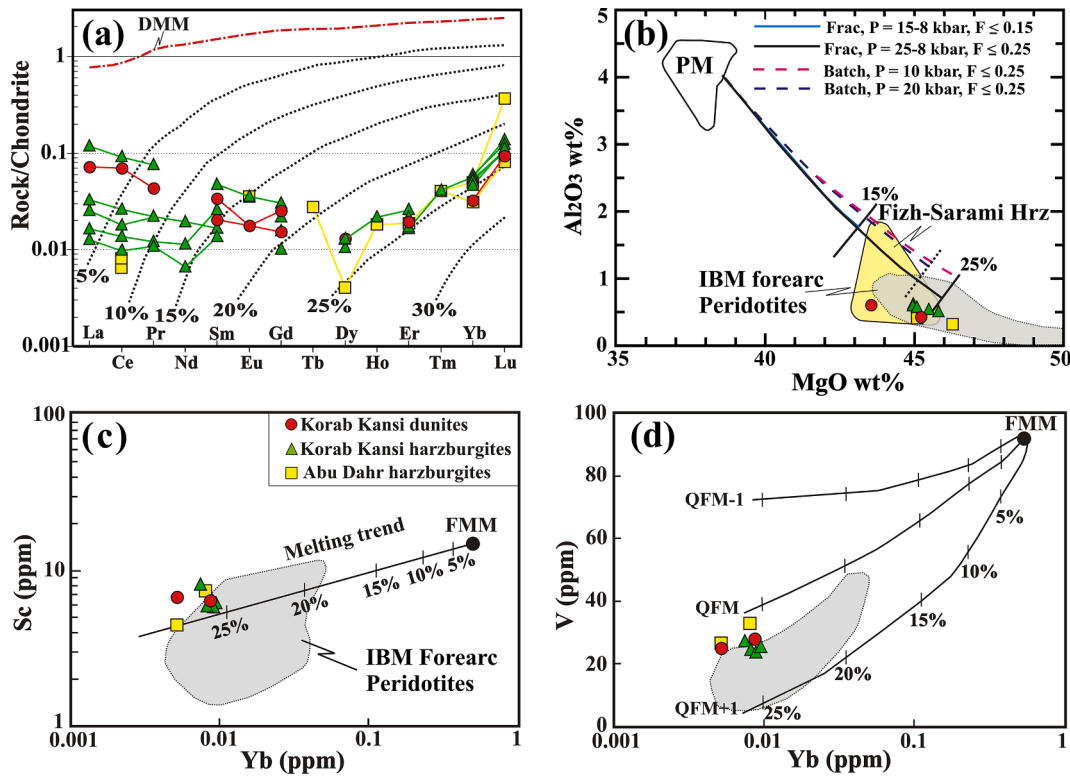
Fig. 12. Estimation of partial melting degrees based on whole-rock chemistry. (**a**) Chondrite-normalized REE patterns of the studied serpentinized peridotites compared with melting curves supporting a source of depleted MORB mantle (DMM) composition in the spinel stability field (De Hoog et al., 2009). The REE composition of depleted MORB mantle (DMM) is after Workman and Hart (2005). (**b**) MgO versus Al_2O_3 diagram for serpentinized peridotites indicating partial melting degree ~20–25% based on Niu (1997) model. Partial melting degrees of isobaric batch melting (broken line) or near-fractional polybaric melting (solid line) are after Niu (1997). The primitive mantle (PM) compositions are after McDonough and Sun (1995) and Niu (1997). The fields of Izu–Bonin–Mariana (IBM) forearc peridotites (Parkinson and Pearce, 1998) and Fizh-Sarami (Oman) harzburgites (Hrz) (Takazawa et al., 2003; Khedr et al., 2014) were used for comparison. (**c, d**) Yb (ppm) versus both Sc and V (ppm) binary diagrams for residual peridotites (Pearce and Parkinson, 1993). Trends in diagrams indicate fractional melting for different oxygen fugacities. FMM (Fertile MORB Mantle) and QFM indicating log fO_2 relative to quartz–fayalite–magnetite buffer (Lee et al., 2003) are used for comparison.

low concentrations of Nb, Ta, Zr and Hf (<0.13 ppm; Table 3) and Nb/Ta and Zr/Hf chondrite-normalized ratios (<0.5) of Abu Dahr and Korab Kansi peridotites indicate that their sub-arc mantle source experienced earlier melt extraction (e.g., Yang and Zhou, 2009). The high Ni/Co ratio (21.4–23.3; Table 3) of ED ophiolitic peridotites, similar to the Ni/Co ratio (21.3–27) of Izu-Bonin-Mariana forearc peridotites (Parkinson and Pearce, 1998), is consistent with formation beneath a Neoproterozoic forearc during subduction initiation. This interpretation is consistent with increasing interpretation of ED ophiolitic peridotites as forming beneath a proto-forearc during subduction initiation, beginning with Azer and Stern (2007).

Opx compositions (Mg#, 0.91–0.93; Al_2O_3, 1.0–2.1 wt%; Cr_2O_3, 0.45–0.8 wt%; CaO, 0.6–3.0 wt%; Table 1; Supplement 2) resemble primary Opx in forearc peridotites (Fig. 5c), especially Abu Dahr Opx, while Korab Kansi Opxs have similar compositions to those in abyssal and forearc peridotites (Fig. 5d, e) (Ohara and Ishii, 1998; Parkinson and Pearce, 1998). These Opxs also show both REE spoon-shaped patterns (Fig. 7a) and spider patterns with positive spikes for U, Nb, Pb and Hf (Fig. 7b), similar to primary Opxs in SSZ peridotites of Tonga (Birner et al., 2007) and SW Turkey (Aldanmaz, 2012).

The examined olivine compositions match olivines in Izu-Ogasawara-Mariana forearc peridotites (Ishii et al., 1992), Qilian forearc harzburgites of NW China (Song et al., 2009), Mugla SSZ peridotites of SW Turkey (Uysal et al., 2012) and forearc serpentinized peridotites from the Central ED of Egypt (Azer and Stern, 2007; Khedr and Arai, 2017) (Fig. 5a, b). The high Fo contents of Korab Kansi and Abu Dahr residual olivine (90.5–92.17; Fig. 5a, 11c) are consistent with olivine Fo (~90–94) of worldwide forearc peridotites (e.g. Bonatti and Michael, 1989; Stern et al., 2004; Khedr and Arai, 2013). In addition, PM-

normalized trace element patterns (Fig. 7b, f) of refractory mantle minerals (e.g. olivine and Opx) are enriched in Li, B, Cs and Pb relative to HFSE (e.g. Nb, Ta, Ti and Zr), supporting a SSZ setting and reflecting the effects of subduction-related fluids on mantle-wedge peridotites (Scambelluri et al., 2006; Khedr et al., 2010; Khedr and Arai, 2017).

The investigated spinel chemistry (Cr#= 0.54–0.75; Mg#= 0.32–0.55; Y_{Fe} < 0.05; TiO_2 < 0.04 wt%) resembles that of primary spinel in Mariana forearc peridotites (Fig. 6f), but we noted that Cr-spinels in Korab Kansi harzburgites share common features of both forearc and back-arc basins or abyssal peridotites (Fig. 6e, f). This high spinel Cr# is also characteristic of depleted forearc mantle peridotites (Ishii et al. 1992; Arai, 1994a; Parkinson and Arculus, 1999) (Fig. 6c-f). Examined spinels also plot on the Cr-Al-Fe ternary diagram in the field of forearc peridotite spinels (Fig. 6a). Spinel REE (Fig. 7g) and trace-element patterns (Fig. 7h) resemble those of Sulu (China) forearc peridotite spinels (Xie et al., 2021).

As previously noted, calculated Abu Dahr melts in equilibrium with Cr-spinel were boninitic (Supplement 2; Fig. 11d). Such melts are commonly generated during subduction (Fig. 13). On the other hand, Korab Kansi melt equilibrated with tholeiitic melts that likely formed during early proto-forearc spreading accompanying subduction initiation due to asthenosphere upwelling and slab rollback (Stern, 2004; Whattam and Stern, 2011; Moghadam et al., 2015; Khedr and Arai, 2017). Tholeiitic low-Ti MORB-like melts are thought to be generated in the earliest stages of subduction initiation via decompression melting of fertile peridotites, while boninitic melts were formed via melting of highly depleted peridotites in the presence of slab-derived fluids (Whattam and Stern, 2011) (Fig. 13). Abu Dahr Cr-spinels plot in the forearc field, while Korab Kansi Cr-spinels lay in the overlapping space

SED ophiolites, Arais (West) to Abu Dahr ophiolite (East)   **SED ophiolites, Korab Kansi (West) to Gerf ophiolite (East)**
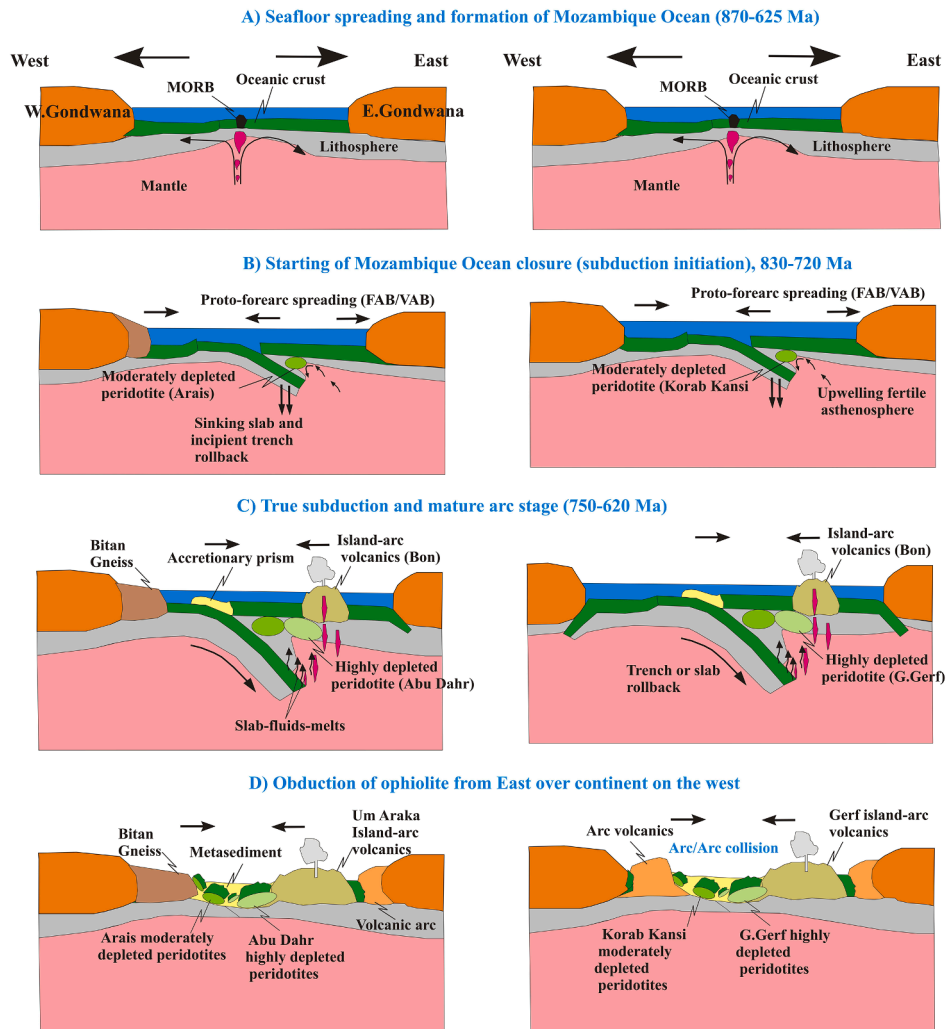

Fig. 13. Schematic sections showing evolution of the SED ophiolites during opening and closure of Mozambique Ocean based on the subduction initiation model (Whattam and Stern, 2011). Gondwana supercontinent assembly and age of Mozambique Ocean opening and closure, as well as subduction are after Kröner and Stern (2004) and Stern and Johnson (2010). Tholeiitic melts were generated in the earliest stages of subduction initiation via decompression melting of fertile peridotites during interaction with the asthenosphere source, forming MORB-like melts, while boninitic melts were formed via melting of depleted peridotites in the presence of sufficient slab-derived fluids during true subduction (Whattam and Stern, 2011). Arais depleted peridotites (Khedr and Arai, 2013) in the west of Abu Dahr and Gerf highly depleted peridotites (Abdel-Karim et al., 2016) in the east of Korab Kansi are used to indicate direction of mantle fertility. BON: boninite, FAB: forearc basalts, VAB: volcanic arc basalts.

between forearc and back-arc basin peridotites (Fig. 6d-f).

As previously noted, Cr-spinels in Korab Kansi harzburgites have lower Cr# than those of Abu Dahr (Supplement 2; Table 2). Korab Kansi Opxs contain more Al$_2$O$_3$ than those of Abu Dahr (Table 1; Fig. 5c-e), suggesting that the Korab Kansi mantle source was less depleted. These relationships suggest that partial melting increased from W to E and from SW to NE (Fig. 13) with 25–40% melting for Korab Kansi peridotites and 30–40% melting for Abu Dahr peridotites (Fig. 6f, 11c, 12). These variations in melt generation suggest early proto-forearc spreading to form the Korab Kansi ophiolite and a more mature proto-arc stage for Abu Dahr peridotites (Fig. 13). Subduction initiation possibly started in the west and/or SW by proto-forearc spreading, and progressed to the east and/or NE (Fig. 1) to a mature arc stage with boninitic melts above an E- or SE-dipping subduction zone (Fig. 13). These considerations suggest increasing mantle fertility from E to W and from NE to SW. Decreasing mantle depletion from W to E is consistent with the Abu Dahr highly depleted peridotites in the east to Arais slightly depleted peridotites (Khedr and Arai, 2013, 2016) in the west (Fig. 13). This parallels the trend of Gerf highly depleted peridotites in

the east (Abdel-Karim et al., 2016) to Korab Kansi depleted peridotites in the west (Figs. 1, 13).

The studied peridotites were generated under oxidizing conditions (Δlog fO$_2$, 0.26–2.58), similar to other SSZ forearc peridotites (Δlog fO$_2$, 0.3–2.0; Parkinson and Arculus, 1999). The wide variations of fO$_2$ (FMQ + 0.26 to FMQ + 2.58; Table 4; Fig. 11a) for SED peridotites may be due to increasing interaction between depleted mantle sources and slab-derived fluids during transitions from incipient arc stage to the mature arc stage during subduction initiation. Δlog fO$_2$ for Abu Dahr (FMQ + 1.7 to FMQ + 2.42) overlaps that of Korab Kansi peridotites (FMQ + 0.26 to FMQ + 2.58) and the significance of this is not yet understood.

We suggest that Abu Dahr and Korab Kansi peridotites formed in association with one or more new subduction zones that closed the Tonian-Cryogenian Mozambique Ocean, culminating in the Ediacaran collision between East and West Gondwanaland (Fig. 13). Large amounts of slab-derived fluids caused extensive melting.

8.4. Chemical changes related to serpentinization and metamorphism

Some Korab Kansi ultramafic rocks converted to prograde peridotites because of contact metamorphism by granitic intrusion (Fig. 2a). Prograde peridotites contain olivine with very high $Fo_{94.9-95.9}$ contents, similar to low-P olivines ($Fo_{92-96.5}$) in Happo-O'ne prograde peridotites, Japan (Khedr and Arai, 2012) (Fig. 5a, b; Table 1; Supplement 2). Olivine is sometimes sieved by fine-dusty magnetite grains, in contrast with primary mantle olivines. Magnetite exsolved during prograde metamorphism of serpentine to low-pressure (metamorphic) olivines. During prograde metamorphism, Fe decreases but Mg increases in metamorphic olivines with high Fo (up to 96.5) (Fig. 5a). Some spinels were metamorphosed to ferritchromite associated with tremolite (Table 2) mainly under greenschist facies. This ferritchromite has higher NiO content (up to 1.16 wt%) relative to primary Cr-spinel (Table 2; Supplement 2), suggesting Ni was released by alteration of olivine and/ or Opx found in contact with Cr-spinel (Khalil and El-Makky, 2008; Marques et al., 2007).

As previously noted, Korab Kansi and Abu Dahr peridotites suffered variable serpentinization (Table 3) but it is unknown when this happened. Serpentinization occurred in two stages: 1) formation of interpenetrating antigorite (Supplement 1), dominant in Korab Kansi serpentinized peridotites; 2) formation of mesh and bastite textured serpentines, composed chiefly of lizardite and chrysotile (Fig. 4e). Variable serpentinization of Korab Kansi and Abu Dahr peridotites is consistent with their high LOI values (7.74–14.43 wt%; Table 3). LOI increases with increasing alteration from harzburgites to dunites, consistent with petrographic studies (Fig. 4). LOI is plotted against selected major and trace elements to evaluate the effects of serpentinization on other chemical changes (Fig. 10). SiO_2, Fe_2O_3 and MgO anti-correlate with LOI (Fig. 10a–f), suggesting mobility during serpentinization. The possible loss of Mg during serpentinization (Snow and Dick, 1995; Niu, 2004; Uysal et al., 2012) can be evaluated by plotting analyzed peridotites on the MgO/SiO_2 versus Al_2O_3/SiO_2 diagram (Fig. 8d). Serpentinized peridotites plot around the terrestrial array (Fig. 8d); hence no significant gain or loss of Si, Mg and Al appears to have occurred during serpentinization. This is consistent with peridotite Mg#, which strongly resembles its olivine Mg# (0.9–0.94) and Opx Mg# (0.9–0.93) (Supplement 2). In contrast, addition of CO_2-rich fluids (Fig. 4i) along shear zones in ultramafic rocks (Fig. 3d, e) forms talc carbonates. Carbonization of peridotites is more extensive for Korab Kansi than for Abu Dahr due to more pervasive deformation by the Hamisana shear zone and strike-slip faults (Fig. 2). Carbonization is more pervasive in harzburgites than dunites and whole-rock compositions of harzburgite are slightly enriched in Ca and Mg (Fig. 10c, e). On the other hand, the good correlation between fluid-mobile element abundances (e.g. B, Li, Sr and Ba) and LOI (Fig. 10g-j) suggests that these elements were added during serpentinization. Therefore, serpentinization can modify the distribution of some trace elements and also can modify the redox state of the system. This agrees with trace element patterns of analyzed peridotites (Fig. 9b) that are enriched in fluid mobile elements (e.g. Pb, B, Li, Rb, Ba and Sr). Higher concentrations of these elements in more serpentinized dunites than in less serpentinized harzburgites (Table 3; Fig. 9b) suggest that the abundance of these elements was controlled by serpentinization processes (Scambelluri et al., 2004; Khedr et al., 2010).

Concentrations of Al, Cr, HFSE and HREE do not correlate with LOI and do not appear to be mobile during serpentinization. Very low concentrations of REE (ΣREE < 0.2 ppm, Table 3) of serpentinized peridotites reflect depleted ultramafic protoliths, mainly harzburgites. On the other hand, LREEs are more mobile and affected by serpentinization. Correlation between ΣLREE and LOI (Fig. 10k) for the studied peridotites supports addition of these elements from serpentinizing fluids. LREEs may have been added to mantle peridotites above a subduction zone and/or during ophiolite obduction (e.g. Paulick et al., 2006; Khedr et al., 2014).

U-shaped REE patterns of Korab Kansi and Abu Dahr serpentinized peridotites (Fig. 9a) may indicate subduction metasomatism and addition of LREE from slab-derived fluids (Scambelluri et al., 2004, 2006; Khedr et al., 2010, 2014) and/or serpentinization (Paulick et al., 2006). Addition of some mobile elements (LREE, B, Pb, Sr, Th; Fig. 9) can also take place during ophiolite emplacement (Delavari et al., 2009).

9. Conclusions

1) Primary olivine, Opx and Cr-spinel in Korab Kansi and Abu Dahr serpentinized peridotites in the SED of Egypt are still retained in these mantle sections, which are mainly harzburgites with subordinate dunites. Minerals and host peridotite compositions suggest that their protoliths were refractory mantle residues (25–40% melting) and represent forearc peridotites.

2) Chromian spinel in SED peridotites was mainly in equilibrium with low-Ti tholeiitic to boninitic melts. These likely formed at a proto-forearc spreading center accompanying extension during subduction initiation.

3) Enrichment of fluid-mobile elements of serpentinized peridotites and their minerals indicates refertilization by fluid–mantle interaction associated with subduction. Large volumes of slab-derived fluids were responsible for extensive melting in the sub-proto forearc mantle.

4) The less-depleted nature of Korab Kansi mantle peridotites relative to those of Abu Dahr may be explained as due to variations of partial melting associated with convergent margin evolution.

5) Variations of partial melting degrees and mantle compositions and the wide range of oxidation state ($\Delta\log fO_2$, FMQ + 0.26– FMQ + 2.58) suggest changing tectonic styles during proto-forearc spreading. Subduction initiation possibly started in the W and/or SW, and progressed to the E and/or NE, forming an E- and/or SE-dipping subduction zone beneath what is now the SED of Egypt.

6) Abu Dahr and Korab Kansi peridotites formed in association with one or more new subduction zones that closed the Tonian-Cryogenian Mozambique Ocean, culminating in the Ediacaran collision between East and West Gondwanaland.

Declaration of Competing Interest

The authors declare that they have no known competing financial interests or personal relationships that could have appeared to influence the work reported in this paper.

Appendix A. Supplementary material

Supplementary data to this article can be found online at https://doi.org/10.1016/j.jseaes.2022.105078.

References

Abdeen, M.M., Abdelghaffar, A.A., 2011. Syn- and post-accretionary structures in the Neoproterozoic Central Allaqi-Heiani suture zone, Southeastern Egypt. Precambrian Res. 185 (3-4), 95–108.

Abdel-Gawad, G.M., 2002. Geological and geochemical characteristics of the mafic-ultramafic rocks of Gabal Korab Kansi area, South Eastern Desert, Egypt. Ph.D. Zagazig University, Thesis, p. 195.

El-Rahman, Y.A., Polat, A., Dilek, Y., Fryer, B., El-Sharkawy, M., Sakran, S., 2009. Geochemistry and tectonic evolution of the Neoproterozoic Wadi Ghadir ophiolite, Eastern Desert. Egypt. Lithos 113 (1-2), 158–178.

Abdel Halim, A.H., Helmy, H.M., Elhaddad, M.A., El–Mahallawi, M.M., Mogessie, A., 2020. Petrology of a Neoproterozoic mantle peridotite–chromitite association from Abu Dahr area, Eastern Desert, Egypt: Infiltration of a boninitic melt in highly depleted harzburgite. J. Afr. Earth Sci. 165, 103816. https://doi.org/10.1016/j.jafrearsci.2020.103816.

Abdel-Karim, A.-A., Ali, S., Helmy, H.M., El-Shafei, S.A., 2016. A fore-arc setting of the Gerf ophiolite, Eastern Desert, Egypt: Evidence from mineral chemistry and geochemistry of ultramafites. Lithos 263, 52–65.

Abdel Khalek, M.L., Takla, M.A., Sehim, A., Hamimi, Z., El–Manawi, A.W., 1992. Geology and tectonic evolution of Wadi Beitan area, southeastern Desert, Egypt. In: First International Conference on Geology of the Arab World, Cairo University, vol. 2, pp. 369–394.

Ahmed, A.H., 2013. Highly depleted harzburgite–dunite–chromitite complexes from the Neoproterozoic ophiolite, south Eastern Desert, Egypt: a possible recycled upper mantle lithosphere. Precambrian Res. 233, 173–192.

Aldanmaz, E., 2012. Trace element geochemistry of primary mantle minerals in spinel-peridotites from polygenetic MOR–SSZ suites of SW Turkey: constraints from an LA-ICP-MS study and implications for mantle metasomatism. Geol. J. 47 (1), 59–76.

Ali, K.A., Azer, M.K., Gahlan, H.A., Wilde, S.A., Samuel, M.D., Stern, R.J., 2010. Age constraints on the formation and emplacement of Neoproterozoic ophiolites along the Allaqi-Heiani Suture, South Eastern Desert of Egypt. Gondwana Res. 18 (4), 583–595.

Ali, K.A., Kröner, A., Hegner, E., Wong, J., Li, S.-Q., Gahlan, H.A., Abu El Ela, F.F., 2015. U-Pb zircon geochronology and Hf–Nd isotopic systematics of Wadi Beitan granitoid gneisses, South Eastern Desert, Egypt. Gondwana Res. 27 (2), 811–824.

Arai, S., 1980. Dunite-harzburgite-chromitite complexes as refractory residue in the Sangun-Yamaguchi zone, western Japan. J. Petrol. 21 (1), 141–165.

Arai, S., 1992. Chemistry of chromian spinel in volcanic rocks as a potential guide to magma chemistry. Mineral. Mag. 56, 173–184.

Arai, S., 1994a. Characterization of spinel peridotites by olivine–spinel compositional relationships: review and interpretation. Chem. Geol. 113 (3-4), 191–204.

Arai, S., 1994b. Compositional variation of olivine-chromian spinel in Mg-rich magmas as a guide to their residual spinel peridotites. J. Volcanol. Geotherm. Res. 59 (4), 279–293.

Arai, S., 1997. Control of wall-rock composition on the formation of podiform chromitites as a result of magma/peridotite interaction. Resour. Geol. 47, 177–187.

Azer, M.K., Khalil, A.E.S., 2005. Petrological and mineralogical studies of pan-African serpentinites at Bir Al-Edeid area, central Eastern Desert. Egypt. J. Afr. Earth Sci. 43 (5), 525–536.

Azer, M., Stern, R.J., 2007. Neoproterozoic serpentinites in the Eastern Desert, Egypt: Fragments of fore-arc mantle. J. Geol. 115, 457–472.

Azer, M.K., Samuel, M.D., Ali, K.A., Gahlan, H.A., Stern, R.J., Ren, M., Moussa, H.E., 2013. Neoproterozoic ophiolitic peridotites along the Allaqi-Heiani suture, south Eastern Desert, Egypt. Mineral. Petrol. 107 (5), 829–848.

Ballhaus, C., Berry, R.F., Green, D.H., 1990. Oxygen fugacity controls in the Earth's upper mantle. Nature 348, 437–440.

Ballhaus, C., Berry, R.F., Green, D.H., 1991. High pressure experimental calibration of the olivine–orthopyroxene–spinel oxygen barometer: implications for the oxidation state of the mantle. Contrib. Miner. Petrol. 107, 27–40.

Barnes, S.J., 2000. Chromite in komatiites, II. Modification during greenschist to mid-amphibolite facies metamorphism. J. Petrol. 41 (3), 387–409.

Barnes, S.J., Roeder, P.L., 2001. The range of spinel compositions in terrestrial mafic and ultramafic rocks. J. Petrol. 42 (12), 2279–2302.

Beccaluva, L., Coltorti, M., Giunta, G., Siena, F., 2004. Tethyan vs. Cordilleran ophiolites: a reappraisal of distinctive tectono-magmatic features of supra-subduction complexes in relation to subduction mode. Tectonophysics 393, 163–174.

Birner, S.K., Warren, J.M., Cottrell, E., Davis, F.A., Kelley, K.A., Falloon, T.J., 2017. Forearc peridotites from Tonga record heterogeneous oxidation of the mantle following subduction initiation. J. Petrol. 58 (9), 1755–1780.

Bonatti, E., Michael, P.J., 1989. Mantle peridotites from continental rifts to ocean basins to subduction zones. Earth Planet. Sci. Lett. 91 (3-4), 297–311.

Brey, G.P., Kohler, T., 1990. Geothermobarometry in four-phase lherzolites II. New thermobarometers, and practical assessment of existing thermobarometers. J. Petrol. 31 (6), 1353–1378.

De Hoog, J.C.M., Janák, M., Vrabec, M., Froitzheim, N., 2009. Serpentinised peridotites from an ultrahigh-pressure terrane in the Pohorje Mts. (Eastern Alps, Slovenia): geochemical constraints on petrogenesis and tectonic setting. Lithos 109 (3-4), 209–222.

De Hoog, J.C.M., Gall, L., Cornell, D.H., 2010. Trace-element geochemistry of mantle olivine and application to mantle petrogenesis and geothermobarometry. Chem. Geol. 270 (1-4), 196–215.

Delavari, M., Amini, S., Saccani, E., Beccaluva, L., 2009. Geochemistry and petrogenesis of mantle peridotites from the Nehbandan Ophiolitic Complex, eastern Iran. J. Appl. Sci. 9, 2671–2687.

Dilek, Y., Thy, P., 2009. Island arc tholeiite to boninitic melt evolution of the Cretaceous Kizildag (Turkey) ophiolite: model for multi-stage early arc–forearc magmatism in Tethyan subduction factories. Lithos 113 (1-2), 68–87.

Dick, H.J.B., Bullen, T., 1984. Chromian spinel as a petrogenetic indicator in abyssal and Alpine-type peridotites and spatially associated lavas. Contrib. Miner. Petrol. 86 (1), 54–76.

Evans, B.W., 2010. Lizardite versus antigorite serpentinite: magnetite, hydrogen, and life (?). Geology 38 (10), 879–882.

Evans, B.W., Frost, B.R., 1975. Chrome-spinel in progressive metamorphism–a preliminary analysis. Geochim. Cosmochim Acta 39 (6-7), 959–972.

Farahat, E.S., Hoinkes, G., Mogessie, A., 2011. Petrogenetic and geotectonic significance of Neoproterozoic suprasubduction mantle as revealed by the Wizer ophiolite complex, Central Eastern Desert, Egypt. Int. J. Earth Sci. (Geol Rundsch) 100 (7), 1433–1450.

Fritz, H., Abdelsalam, M., Ali, K.A., Bingen, B., Collins, A.S., Fowler, A.R., Ghebreab, W., Hauzenberger, C.A., Johnson, P.R., Kusky, T.M., Macey, P., Muhongo, S., Stern, R.J., Viola, G., 2013. Orogen styles in the East African Orogen: A review of the Neoproterozoic to Cambrian tectonic evolution. J. Afr. Earth Sci. 86, 65–106.

Furnes, H., de Wit, M., Dilek, Y., 2014. Four billion years of ophiolites reveal secular trends in oceanic crust formation. Geosci. Front. 5 (4), 571–603.

Gahlan, H.A., Azer, M.K., Khalil, A.E.S., 2015. The Neoproterozoic Abu Dahr ophiolite south Eastern Desert Egypt, petrological characteristics and tectonomagmatic evolution. Mineral. Petrol. 109 (5), 611–630.

Godard, M., Jousselin, D., Bodinier, J.L., 2000. Relationships between geochemistry and structure beneath a paleo-spreading centre: a study of the mantle section in the Oman ophiolite. Earth Planet. Sci. Lett. 180, 133–148.

Greiling, R.O., Abdeen, M.M., Dardir, A.A., El Akhal, H., El Ramly, M.F., El Din Kamal, G. M., Osman, A.F., Rashwan, A.A., Rice, A.H.N., Sadek, M.F., 1994. A structural synthesis of the Proterozoic Arabian-Nubian Shield in Egypt. Geol. Rundsch. 83 (3), 484–501.

Grove, T., Chatterjee, N., Parman, S., Medard, E., 2006. The influence of H2O on mantle wedge melting. Earth Planet. Sci. Lett. 249 (1-2), 74–89.

Hart, S.R., Zindler, A., 1986. In search of a bulk-Earth composition. Chem. Geol. 57 (3-4), 247–267.

Hellebrand, E., Snow, J.E., Dick, H.J.B., Hofmann, A.W., 2001. Coupled major and trace elements as indicators of the extent of melting in mid-ocean-ridge peridotites. Nature 410 (6829), 677–681.

Hickey, R.L., Frey, F.A., 1982. Geochemical characteristics of boninite series volcanics: implications for their source. Geochim. Cosmochim Acta 46 (11), 2099–2115.

Hirose, K., Kawamoto, T., 1995. Hydrous partial melting of lherzolite at 1 GPa: The effect of H2O on the genesis of basaltic magmas. Earth Planet. Sci. Lett. 133 (3-4), 463–473.

Ishii, T., Robinson, P.T., Maekawa, H., Fiske, R., 1992. Petrological studies of peridotites from diapiric serpentinite seamounts in the Izu-Ogasawara-Mariana Forearc, Leg 125. In: Proc. Ocean Drilling Progr.: Sci. Results, vol. 125, pp. 445–485.

Jagoutz, E., Palme, H., Baddenhausen, H., Blum, K., Cendales, M., Dreibus, G., Spettel, B., Lorenz, V., Wanke, H., 1979. The abundances of major, minor and trace elements in the earth's mantle as derived from primitive ultramafic nodules. In: Proceedings of the tenth Lunar and Planet. Sci., vol. 2, pp. 2031–2050.

Jan, M.Q., Windley, B.F., 1990. Chromian spinel–silicate chemistry in ultramafic rocks of the Jijal Complex, Northwest Pakistan. J. Petrol. 31 (3), 667–715.

Jaques, A.L., Green, D.H., 1980. Anhydrous melting of peridotite at 0–15 Kb pressure and the genesis of tholeiitic basalts. Contrib. Miner. Petrol. 73 (3), 287–310.

Jennings, E.S., Holland, T.J.B., 2015. A simple thermodynamic model for melting of peridotite in the system NCFMASOCr. J. Petrol. 56 (5), 869–892.

Kamenetsky, V.S., Crawford, A.J., Meffre, S., 2001. Factors controlling chemistry of magmatic spinel: An empirical study of associated olivine, Cr-spinel and melt inclusions from primitive rocks. J. Petrol. 42, 655–671.

Khalil, A.E.S., Azer, M.K., 2007. Supra-subduction affinity in the Neoproterozoic serpentinites in the Eastern Desert, Egypt: evidence from mineral composition. J. Afr. Earth Sci. 49 (4-5), 136–152.

Khalil, K.I., El-Makky, A.M., 2008. Alteration Mechanisms of Chromian-Spinel during Serpentinization at Wadi Sifein Area, Eastern Desert, Egypt. Resour Geol 59 (2), 194–211.

Khedr, M.Z., Arai, S., 2010. Hydrous peridotites with Ti-rich chromian spinel as a low-temperature forearc mantle facies: evidence from the Happo-O'ne metaperidotites (Japan). Contrib. Miner. Petrol. 159 (2), 137–157.

Khedr, M.Z., Arai, S., 2012. Petrology and geochemistry of prograde deserpentinized peridotites from Happo-O'ne, Japan: evidence of element mobility during deserpentinization. J. Asian Earth Sc. 43, 150–163.

Khedr, M.Z., Arai, S., 2013. Origin of Neoproterozoic ophiolitic peridotites in south Eastern Desert, Egypt, constrained from primary mantle mineral chemistry. Mineral. Petrol. 107 (5), 807–828.

Khedr, M.Z., Arai, S., 2016. Chemical variations of mineral inclusions in Neoproterozoic high-Cr chromitites from Egypt: evidence of fluids during chromitite genesis. Lithos 240-243, 309–326.

Khedr, M.Z., Arai, S., 2017. Peridotite-chromitite complexes in the Eastern Desert of Egypt: insight into Neoproterozoic sub-arc mantle processes. Gondwana Res. 52, 59–79.

Khedr, M.Z., Arai, S., Tamura, A., Morishita, T., 2010. Clinopyroxenes in high-P metaperidotites from Happo-O'ne, central Japan: implications for wedge-transversal chemical change of slab-derived fluids. Lithos 119 (3-4), 439–456.

Khedr, M.Z., Arai, S., Python, M., Tamura, A., 2014. Chemical variations of abyssal peridotites in the central Oman ophiolite: evidence of oceanic mantle heterogeneity. Gondwana Res. 25 (3), 1242–1262.

Khedr, M.Z., El-Awady, A., Arai, S., Hauzenberger, C.h., Tamura, A., Stern, J., Morishita, T., 2020. Petrogenesis of the ~740 Ma Korab Kansi mafic-ultramafic intrusion, South Eastern Desert of Egypt: Evidence of Ti-rich ferropicritic magmatism. Gondwana Res. 82, 48–72.

Kodolányi, J., Pettke, T., Spandler, C., Kamber, B.S., Gméling, K., 2012. Geochemistry of ocean floor and fore-arc serpentinites: constraints on the ultramafic input to subduction zones. J. Petrol. 53 (2), 235–270.

Kröner, A., Stern, R.J., 2004. Pan-African orogeny. Encyclopedia of. Geology 1, 1–12.

Kroner, A., Todt, W., Hussein, I., Mansour, M., Rashwan, A., 1992. Dating of late Proterozoic ophiolites in Egypt and the Sudan using the single grain zircon evaporation technique. Precambrian Res. 59 (1-2), 15–32.

Kusky, T.M., Ramadan, T.M., 2002. Structural controls on Neoproterozoic mineralization in the South Eastern Desert, Egypt: an integrated field, Landsat TM, and SIR C/X SAR approach. J. Afr. Earth Sci. 35 (1), 107–121.

Lee, C.T.A., Brandon, A.D., Norman, M., 2003. Vanadium in peridotites as a proxy of Paleo-fO$_2$ during partial melting, prospects, limitations and implications. Geochim. Cosmochim Acta 67, 3045–3064.

Lian, D., Yang, J., Dilek, Y., Rocholl, A., 2019. Mineralogy and geochemistry of peridotites and chromitites in the Aladag Ophiolite (southern Turkey), melt evolution of the Cretaceous Neotethyan mantle. J. Geol. Soc. 176 (5), 958–974. https://doi.org/10.1144/jgs2018-060.

Marocchi, M., Hermann, J., Morten, L., 2007. Evidence for multi-stage metasomatism of chlorite-amphibole peridotites (Ulten Zone, Italy): Constraints from trace element compositions of hydrous phases. Lithos 99 (1-2), 85–104.

Marques, A.F.A., Barriga, F.J.A.S., Scott, S.D., 2007. Sulfide mineralization in an ultramafic-rock hosted seafloor hydrothermal system: From serpentinization to the formation of Cu–Zn–(Co)-rich massive sulfides. Mar. Geol. 245 (1-4), 20–39.

Matsukage, K.N., Kubo, K., 2003. Chromian spinel during melting experiments of dry peridotite KLB-1) at 1.0–2.5 GPa. Am. Min. 88 (8-9), 1271–1278.

Maurel, C., Maurel, P., 1982. Etude experimentale de la distribution de l'aluminiu mentre bain silicate basique et spinelle chromifere. Implications petrogenetiques: teneur en chrome des spinelles. Bull. Minéral. 105, 197–202.

McDonough, W.F., Sun, S.-s., 1995. The composition of the Earth. Chem. Geol. 120 (3-4), 223–253.

Moghadam, H.S., Khedr, M.Z., Arai, S., Stern, R.J., Ghorbani, G., Tamura, A., Ottley, C.J., 2015. Arc-related harzburgite–dunite–chromitite complexes in the mantle section of the Sabzevar ophiolite, Iran: a model for formation of podiform chromitites. Gondwana Res. 27, 575–593.

Moussa, E.M.M., Stern, R.J., Manton, W.I., Ali, K.A., 2008. SHRIMP zircon dating and Sm/Nd isotopic investigations of Neoproterozoic granitoids, Eastern Desert, Egypt. Precambrian Res. 160 (3-4), 341–356.

Niu, Y., 1997. Mantle melting and melt extraction processes beneath ocean ridges: Evidence from abyssal peridotites. J. Petrol. 38 (8), 1047–1074.

Niu, Y., 2004. Bulk-rock major and trace element compositions of abyssal peridotites, implications for mantle melting, melt extraction and post–melting processes beneath mid-ocean ridges. J. Petrol. 45 (12), 2423–2458.

Ohara, Y., Ishii, T., 1998. Peridotites from southern Mariana forearc: heterogeneous fluids supply in mantle wedge. Isl. Arc 7, 541–558.

Parkinson, I.J., Pearce, J.A., 1998. Peridotites from the Izu–Bonin–Mariana forearc (ODP Leg125): evidence for mantle melting and melt–mantle interaction in a suprasubduction zone setting. J. Petrol. 39 (9), 1577–1618.

Parkinson, I.J., Arculus, R.J., 1999. The redox state of subduction zones: insights from arc-peridotites. Chem. Geol. 160 (4), 409–423.

Parkinson, I.J., Arculus, R.J., Eggins, S.M., 2003. Peridotite xenoliths from Grenada, Lesser Antilles Island Arc. Contrib. Miner. Petrol. 146 (2), 241–262.

Paulick, H., Bach, W., Godard, M., De Hoog, J.C.M., Suhr, G., Harvey, J., 2006. Geochemistry of abyssal peridotites (Mid-Atlantic Ridge, 15_200N, ODP Leg209): implications for fluid/rock interaction in slow spreading environments. Chem. Geol. 234, 179–210.

Pearce, J.A., Parkinson, I.J., 1993. Trace element models for mantle melting: application to volcanic arc petrogenesis. Geol. Society, London, Special Publ. 76 (1), 373–403.

Pearce, J.A., Lippard, S.J., Stern, R., 1984. Characteristics and tectonic significance of supra-subduction zone ophiolites. In: Kokelaar, B.P., Howells, M.F. (Eds.), Marginal Basin Geology. Geol. Soc. Lond., vol. 16, pp. 77–94.

Pearce, J.A., Barker, P.F., Edwards, S.J., Parkinson, I.J., Leat, P.T., 2000. Geochemistry and tectonic significance of peridotites from the South Sandwich arc-basin system, South Atlantic. Contrib. Miner. Petrol. 139 (1), 36–53.

Rogkala, A., Petrounias, P., Tsikouras, B., Hatzipanagiotou, K., 2017. New occurrence of pyroxenites in the Veria-Naousa ophiolite (North Greece), implications on their origin and petrogenetic evolution. Geosciences 7, 92. https://doi.org/10.3390/geosciences7040092.

Rolland, Y., Picard, C., Pecher, A., Lapierre, H., Bosch, D., Keller, F., 2002. The Ladakh arc of NW Himalaya-slab melting and melt-mantle interaction during fast northward drift of Indian plate. Chem. Geol. 182, 139–178.

Sack, R.O., Ghiorso, M.S., 1991. Chromian spinel as petrogenetic indicators: thermodynamics and petrological applications. Am. Min. 76, 827–847.

Santos, J.F., Schärer, U., Gil ibarguchi, J.I., Girardeau, J., 2002. Genesis of pyroxenite-rich peridotite at Cabo Ortegal (NW Spain), geochemical and Pb-Sr-Nd isotope data. J. Petrol. 43 (1), 17–43.

Scambelluri, M., Müntener, O., Ottolini, L., Pettke, T.T., Vannucci, R., 2004. The fate of B, Cl and Li in the subducted oceanic mantle and in the antigorite breakdown fluids. Earth Planet. Sci. Lett. 222 (1), 217–234.

Scambelluri, M., Hermann, J., Morten, L., Rampone, E., 2006. Melt-versus fluid-induced metasomatism in spinel to garnet wedge peridotites (Ulten Zone, Eastern Italian Alps): clues from trace element and Li abundances. Contrib. Miner. Petrol. 151 (4), 372–394.

Shackleton, R.M., 1994. Review of late Proterozoic sutures, ophiolitic mélanges and tectonics of eastern Egypt and North Sudan. Geol. Rundsch. 83, 537–546.

Snow, J.E., Dick, H.J.B., 1995. Pervasive magnesium loss by marine weathering of peridotite. Geochim. Cosmochim Acta 59 (20), 4219–4235.

Song, S., Su, Li., Niu, Y., Lai, Y., Zhang, L., 2009. CH4 inclusions in orogenic harzburgite: evidence for reduced slab fluids and implication for redox melting in mantle wedge. Geochim. Cosmochim Acta 73 (6), 1737–1754.

Stern, R., 2004. Subduction initiation: spontaneous and induced. Earth Planet. Sci. Lett. 226 (3-4), 275–292.

Stern, R.J., Hedge, C.E., 1985. Geochronologic constraints on late Precambrian crustal evolution in the Eastern Desert of Egypt. Am. J. Sci. 285, 97–127.

Stern, R.J., Johnson, P., 2010. Continental lithosphere of the Arabian Plate: a geologic, petrologic, and geophysical synthesis. Earth Sci. Rev. 101 (1-2), 29–67.

Stern, R.J., Johnson, P.R., Kröner, A., Yibas, B., 2004. Neoproterozoic ophiolites of the Arabian–Nubian Shield. In: Kusky, T.M. (Eds.) Precambrian ophiolites and related rocks. Developments in Precambrian Geol. vol. 13, pp. 95–128.

Szilas, K., van Hinsberg, V., McDonald, I., Næraa, T., Rollinson, H., Adetunji, J., Bird, D., 2018. Highly refractory Archaean peridotite cumulates: Petrology and geochemistry of the Seqi Ultramafic Complex, SW Greenland. Geosci. Front. 9 (3), 689–714.

Takahashi, E., Uto, K., Schilling, J.G., 1987. Primary magma compositions and Mg/Fe ratios of their mantle residues along Mid-Atlantic Ridge 29 N to 73 N. Technical Reports Institute for Study of the Earth's Interior Okayama University Ser A 9, 1–14.

Takazawa, E., Okayasu, T., Satoh, K., 2003. Geochemistry and origin of the basal lherzolites from the northern Oman ophiolite (northern Fizh block). Geochem. Geophys. Geosyst. 4, 1021. https://doi.org/10.1029/2001GC000 232.

Uysal, İ., Ersoy, Y., Karslı, O., Dilek, Y., Sadıklar, M.B., Ottley, C.J., Tiepolo, M., Meisel, T., 2012. Coexistence of abyssal and ultra–depleted SSZ type mantle peridotites in a neo–Tethyan ophiolite in SW Turkey, constrains from mineral composition, whole rock geochemistry (major–trace–REE–PGE) and Re–Os isotope systematics. Lithos 132, 50–69.

Whattam, S.A., Stern, R.J., 2011. The 'subduction initiation rule': a key for linking ophiolites, intra-oceanic forearcs and subduction initiation. Contrib. Miner. Petrol. 162 (5), 1031–1045.

Workman, R.K., Hart, S.R., 2005. Major and trace element composition of the depleted MORB mantle (DMM). Earth Planet. Sci. Lett. 231 (1-2), 53–72.

Xie, Z., Hattori, K., Dong, Y., Wang, J., 2021. In situ characterization of forearc serpentinized peridotite from the Sulu ultrahigh-pressure terrane: Behavior of fluid-mobile elements in continental subduction zone. Geosci Front 12 (4), 101139. https://doi.org/10.1016/j.gsf.2021.101139.

Yang, S.H., Zhou, M.F., 2009. Geochemistry of the ∼ 430-Ma Jingbulake mafic-ultramafic intrusion in Western Xinjiang, NM China: implications for subduction related magmatism in the South Tianshan orogenic belt. Lithos 113, 259–273.

Youssef, M.M., 2003. Structural setting of central and south Egypt. An overview. Micropaleontology 49 (Suppl_1), 1–13.

Zimmer, M., Kröner, A., Jochum, K.P., Reischmann, T., Todt, W., 1995. The Gabal Gerf complex: A Precambrian N-MORB ophiolite in the Nubian Shield, NE Africa. Chem. Geol. 123 (1-4), 29–51.